

# Colors with plasmonic nanostructures: A full-spectrum review

Cite as: Appl. Phys. Rev. **6**, 041308 (2019); <https://doi.org/10.1063/1.5110051>

Submitted: 14 May 2019 . Accepted: 16 September 2019 . Published Online: 25 October 2019

Maowen Song, Di Wang , Samuel Peana , Sajid Choudhury, Piotr Nyga , Zhaxylyk A. Kudyshev, Honglin Yu, Alexandra Boltasseva, Vladimir M. Shalaev, and Alexander V. Kildishev 

## COLLECTIONS

 This paper was selected as Featured



[View Online](#)



[Export Citation](#)



[CrossMark](#)

## ARTICLES YOU MAY BE INTERESTED IN

[Ion irradiation of III-V semiconductor surfaces: From self-assembled nanostructures to plasmonic crystals](#)

Applied Physics Reviews **6**, 041307 (2019); <https://doi.org/10.1063/1.5079908>

[Charge transfer plasmons: Recent theoretical and experimental developments](#)

Applied Physics Reviews **4**, 021104 (2017); <https://doi.org/10.1063/1.4982890>

[Active meta-optics and nanophotonics with halide perovskites](#)

Applied Physics Reviews **6**, 031307 (2019); <https://doi.org/10.1063/1.5107449>



The banner features the journal logo (a stylized 'A' and 'P' in blue and yellow) and the title "Applied Physics Reviews" in white. To the right is a yellow ribbon badge with the text "Journal Impact Factor 12.750". Below the title is the call-to-action "Submit your original research today!" and a "LEARN MORE >>>" button.

# Colors with plasmonic nanostructures: A full-spectrum review

Cite as: Appl. Phys. Rev. **6**, 041308 (2019); doi: [10.1063/1.5110051](https://doi.org/10.1063/1.5110051)

Submitted: 14 May 2019 · Accepted: 16 September 2019 ·

Published Online: 25 October 2019



[View Online](#)



[Export Citation](#)



[CrossMark](#)

Maowen Song,<sup>1,2</sup> Di Wang,<sup>1</sup> Samuel Peana,<sup>1</sup> Sajid Choudhury,<sup>1</sup> Piotr Nyga,<sup>1,3</sup> Zhaxylyk A. Kudyshev,<sup>1</sup> Honglin Yu,<sup>2</sup> Alexandra Boltasseva,<sup>1</sup> Vladimir M. Shalaev,<sup>1</sup> and Alexander V. Kildishev<sup>1,a)</sup>

## AFFILIATIONS

<sup>1</sup>School of Electrical & Computer Engineering, Birck Nanotechnology Center, Purdue University, 1205 West State Street, West Lafayette, Indiana 47907, USA

<sup>2</sup>Key Lab of Optoelectronic Technology and Systems of Education Ministry of China, Chongqing University, Chongqing 400044, China

<sup>3</sup>Institute of Optoelectronics, Military University of Technology, 2 gen. Sylwestra Kaliskiego Street, Warsaw 00-908, Poland

<sup>a)</sup>Author to whom correspondence should be addressed: [kildishev@purdue.edu](mailto:kildishev@purdue.edu)

## ABSTRACT

Since ancient times, plasmonic structural coloring has inspired humanity; glassmakers achieved vibrant colors by doping glass with metal nanoparticles to craft beautiful objects such as the Roman Lycurgus cup and stained glass. These lovely color filtering effects are a consequence of the resonant coupling of light and free electrons in metal nanoparticles, known as surface plasmons. Thanks to the continuing improvement of nanofabrication technology, the dimensions of nanoparticles and structures can now be precisely engineered to form “optical nanoantennas,” allowing for control of optical response at an unprecedented level. Recently, the field of plasmonic structural coloring has seen extensive growth. In this review, we provide an up-to-date overview of various plasmonic color filtering approaches and highlight their uses in a broad palette of applications. Various surface plasmon resonance modes employed in the plasmonic color filtering effect are discussed. We first review the development of the pioneering static plasmonic colors achieved with invariant optical nanoantennas and ambient environment, then we address a variety of emerging approaches that enable dynamic color tuning, erasing, and restoring. These dynamic color filters are capable of actively changing the filtered colors and carrying more color information states than the static systems. Thus, they open an avenue to high-density data storage, information encryption, and plasmonic information processing. Finally, we discuss the challenges and future perspectives in this exciting research area.

© 2019 Author(s). All article content, except where otherwise noted, is licensed under a Creative Commons Attribution CC BY) license <http://creativecommons.org/licenses/by/4.0/>). <https://doi.org/10.1063/1.5110051>

## TABLE OF CONTENTS

I. INTRODUCTION .....	1
II. COLOR MAPPING WITH THE CIE DIAGRAM .....	2
III. STATIC PLASMONIC COLORS .....	4
A. Gratings and periodic arrays.....	4
B. Subwavelength nanohole array .....	6
C. Hybridized nanohole and nanodisk arrays.....	9
IV. DYNAMICALLY TUNABLE PLASMONIC COLORS .	10
A. Polarization tuning.....	10
B. Electrical tuning.....	12
C. Temperature tuning and laser-induced plasmonic coloration .....	13
D. Chemical tuning .....	15
E. Mechanical tuning.....	17

F. MEMS and NEMS tunable plasmonic devices .....	19
V. OUTLOOK AND CONCLUSIONS .....	21
A. Applications and outlook .....	21
B. Conclusions .....	21

## I. INTRODUCTION

In contrast to active colors generated from light sources with limited bandwidths, passive colors arise from light-matter interaction and are generated when particular wavelength ranges from a broadband (white) light source are removed. In our daily life, the most commonly used materials to render colors are dyes and pigments. These materials absorb a part of the visible spectrum and reflect the remaining part to form colors. Dyes and pigments find usage in a significant fraction of industrialized products because they offer vibrant coloration

irrespective of the incident illumination and viewing angle.<sup>1–5</sup> However, they are not chemically stable at high temperatures and bleach when exposed to intense ultraviolet (UV) illumination. Also, most dyes and pigments are composed of toxic materials, causing tremendous problems in their recycling process. However, most importantly, dyes and pigments can hardly be used in advanced color display and spectral imaging devices that require high spatial resolution—their optical performance, based on volumetric absorption, dramatically deteriorates once particle dimensions fall below the micrometer scale. These drawbacks call for new color generation material platforms with greater chemical stability, lower toxicity, and higher resolution for novel demanding applications.

Photonic crystals or dielectric multilayer structures can also generate colors. Some naturally occurring structures are fine enough to cause interference of the visible light and produce the colorful appearance of amazing creatures around us.<sup>6–14</sup> For example, morpho butterflies have multiple layers of cuticles and air in their wings, which reflect beautiful shimmering blue shades, and beetles' plate-sutured exoskeletons scatter glistening iridescent colors. However, such dielectric nanostructures are of micrometer-scale dimensions, much larger than the diffraction limit. Artificial dielectrics, dielectric metamaterials, and dielectric metasurfaces can also generate structured colors with dielectric scattering elements smaller than the free-space wavelength of light. Unfortunately, their spatial resolution and color quality are limited by the low refractive index and relatively low absorption/scattering cross section achievable for most small dielectric nanoparticles/structures in the visible. Metallic nanostructures, which are known for their large resonant absorption and scattering cross sections, appear to be promising candidates to alleviate these problems.

A large number of historic artworks made with metallic colorants, such as the Celtic red enamels,<sup>15</sup> Roman Lycurgus Cup,<sup>16</sup> stained glass windows,<sup>17</sup> and lusterware have attracted attention from scientists. Investigations reveal that the red color of the glasses, developed in the late Bronze Age (1200–1000 BC) from Italy, is caused by the trace amount of copper nanoparticles,<sup>18,19</sup> as are the colors of the Celtic red enamels dated from 400 to 100 BC.<sup>20</sup> Besides copper, gold and silver nanoparticles are also identified in Roman glasses. One example is the well-known Roman Lycurgus Cup dated to the 4th Century AD.<sup>16</sup> The most remarkable feature of this cup is its dichroic behavior—the cup exhibits a ruby-red color when a white light source illuminates it from inside the cup, and a jade-green color when the same light reflects off it, which is a result of the distinct transmission and scattering spectra modified by the metallic nanoparticles embedded in the glass. The Middle Ages (5th Century AD–15th Century AD) saw the emergence of stained glass and a special type of glazed ceramic now known as lusterware.<sup>21</sup> All the colors of these historic artifacts result from the surface plasmon modes arising from the light interaction with the constituent metallic nanoparticles.

Surface plasmons are collective free electron oscillations that exist at the interface between metal and dielectric materials.<sup>22</sup> When the light of select wavelength strikes a metallic nanoparticle, the electric field of the light drives the metal's free electrons to resonantly oscillate inside the particle, leading to strong optical absorption.<sup>23,24</sup> Such resonance is termed localized surface plasmon resonance (LSPR).<sup>25</sup> LSPR modes exhibit the unparalleled capability to confine light to deep-subwavelength volume. As a result, LSPR-based color filters have attracted tremendous attention because of their extremely high spatial

resolution. Other appealing features such as long-term durability, fabrication simplicity, and large viewing-angle tolerance already promise great potential for optical elements based on plasmonic colors in high-resolution color printing, high-density data storage, and chromatic displays. Recent advancement of nanofabrication technology prompts a leap in the plasmonic color technology; the shape and dimensions of the nanoparticles can be precisely controlled, and intricate architectures can be made with smaller footprints. For example, metallic nano-disks raised above a holey reflector are presented as an effective approach to enhance the spatial resolution to an unprecedented value of  $\sim 100\,000$  dots per inch (dpi).<sup>26</sup> More interestingly, researchers have invented ways to dynamically tune LSPR-filtered colors, and studies in this area have thrived in recent decades.<sup>27–31</sup> In contrast to the static plasmonic colors, two or more color information states can be encoded into one dynamically tunable nanopixel, a feature of significant importance to address the increasing demand for novel optical engineering paradigms such as switchable display, optical steganography, and encryption.

This article reviews the recent advancements in the field of plasmonic colors enabled by metallic nanostructures with the focus on the evolution from devices with static structural plasmonic colors to systems with dynamically tunable colors. The review is organized as follows: Sec. II presents plasmonic color mapping in the diagram made by the International Commission on Illumination (CIE). Sections III and IV focus on static and dynamic plasmonic color filters, respectively. In each section, different mechanisms developed for color control are introduced in detail. The potential applications of various plasmonic color filters are outlined in Sec. V, in which we also provide an outlook and concluding remarks as well as discuss the existing challenges in this research area.

## II. COLOR MAPPING WITH THE CIE DIAGRAM

Color is not a property of electromagnetic radiation but a subjective perception of an observer. That is why it is not straightforward to identify the direct relationship between illumination light intensity  $I(\lambda)$ , the spectrum of reflected light by the object  $R(\lambda)$ , and the color identified by the observer [Fig. 1(a)]. Within this section, we will introduce the basic ideas of the color mapping theory.

Colors are observed when light interacts with objects and the interacted light changes its spectrum through wavelength-dependent absorption, reflection, or refraction. The color of the objects depends on the type of light source. Figure 1(b) shows three different spectra of white light sources typically used in experiments or our everyday life: a tricolor fluorescent lamp (solid), incandescent source (dotted), and white-light light-emitting diode (LED) (dashed). The reflected light interacts with the human eye, which senses color with the help of cone cells—the photoreceptors. Three types of cone cells exist in the eye that respond to different wavelength stimuli, with peak wavelengths of 564–580 nm, 534–545 nm, and 420–440 nm.<sup>32</sup> Human color perception is, therefore, an additive combination of the stimulation of three types of cone cells. Consequently, all color stimuli can be reproduced by mixing three appropriately chosen primaries, which effectively form the specification of the color, and any color can be objectively described by a mixed set of values associated with the quantity of primary illumination. These sets of values are called tristimulus values. CIE 1931 defines a color space map that is described as a range of physically produced colors to the tristimulus values. The standard also

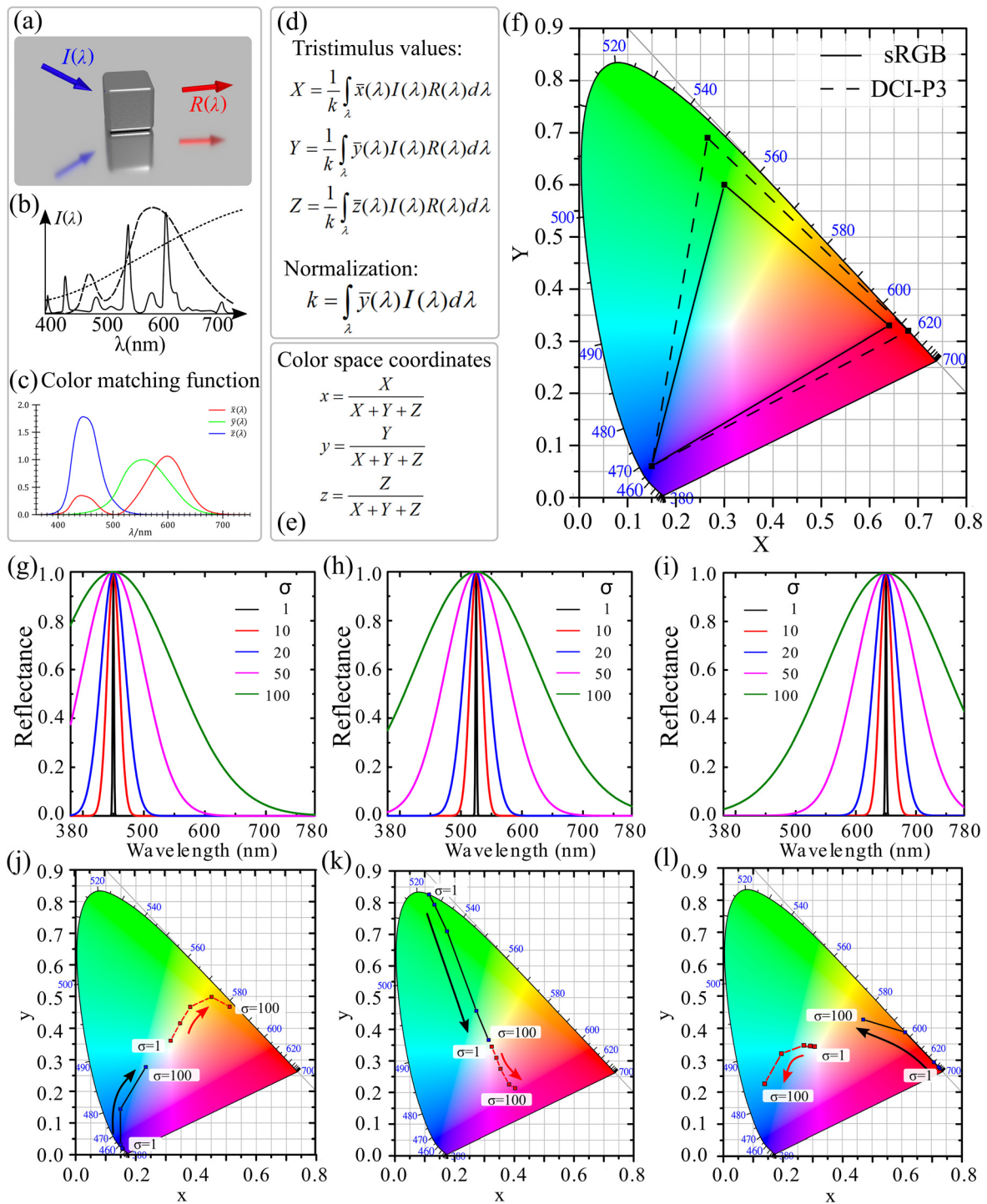


**FIG 1** a) Schematics of reflection of the incident light from the object; b) three types of white light sources: a tricolor fluorescent lamp (solid), incandescent source (dotted), and white-light LED (dashed); c) color matching functions  $\bar{x}(l)$ ,  $\bar{y}(l)$ ,  $\bar{z}(l)$  defined by CIE 1931; d) integral relations between tristimulus values and illumination/reflection spectra; e) definition of color space coordinates, calculated based on tristimulus values; f) sRGB (solid) and DCI-P3 (dashed) color spaces on CIE 1931 diagram; g)– i) customized reflection spectra for additive colors (blue, green, and red) with different linewidths. Standard deviation  $\sigma$  varies from 1 to 100, corresponding to the linewidth broadening from 2.355 to 235.5 nm. j)– l) Mapping the customized reflection spectra in g), h), and i) to the chromaticity coordinates  $x$ ,  $y$  in the CIE 1931 diagram, respectively. The red curves show the corresponding colors formed by subtractive Gaussian spectra.

defines color matching functions  $[\bar{x}(\lambda), \bar{y}(\lambda), \bar{z}(\lambda)]$  as a numerical description of the spectral sensitivity curves of the observer [Fig. 1(c)]. CIE evaluates the color-matching functions by a linear transformation of the observer sensitivity of different colors. Detailed description of the origin and development of the color matching functions can be found in Ref. 33. For a given relative spectral power distribution of the illuminating light  $I(\lambda)$ , and reflection spectrum  $R(\lambda)$ , the tristimulus values (X, Y, Z) can be computed by the integral relation outlined in Fig. 1(d), where  $K = \int \bar{y}(\lambda) I(\lambda) d\lambda$  is a normalizing factor, integrated across the wavelength range of 380–780 nm.

To provide a perceptive color map, the CIE created a two-dimensional chromaticity diagram to show the different color stimuli. Each point (x,y) on the diagram represents a color described by its tristimulus value. The relation between the coordinates and the tristimulus values is shown in Fig. 1(e). In 1996, a convenient color model for computer graphics and monitor displays—the standard Red Green Blue (sRGB)—was created by the Microsoft Corporation and the Hewlett-Packard Company in a cooperative effort.<sup>34</sup> The sRGB is an additive color space, in that any color within the sRGB color space [the black triangle in Fig. 1(f)] can be represented by a non-negative addition of the three primary colors red, green, and blue, the three apexes of the sRGB triangle in Fig. 1(f). This color space goes particularly well with computer color displays because colors in the computer monitors are constructed by adjusting the relative intensities of the RGB light emitters. However, as can be seen from Fig. 1(f), the sRGB color space covers only a relatively limited portion of the CIE diagram, lacking specifically highly saturated blue and green colors. In 2010, the Digital Cinema Initiatives organization defined the DCI-P3 color space [see a dashed triangle in Fig. 1(f)], with expanded color gamut compared to the sRGB color space.<sup>35</sup> Owing to the recent development of display technology, specifically organic light-emitting diode (OLED) and quantum dot light-emitting diode (QLED) displays, more saturated colors can be generated. The DCI-P3 color space has since gained burgeoning popularity and has become the color standard among many display industry leaders such as Apple Inc.<sup>36</sup> and Samsung Electronics Co.<sup>37</sup>

Another widely used color model is the CMYK color model, where the four letters stand for cyan, magenta, yellow, and black. Contrary to sRGB, CMYK is a subtractive color model because cyan, magenta, and yellow are obtained by subtracting red, green, and blue from white light, respectively. In additive color models such as sRGB, white color results from the additive combination of primaries with maximum relative intensity, whereas in the CMYK color model, the additive combination of primaries results in black color. Due to its subtractive nature, the CMYK color model works best for color printing because inks render colors by absorbing a certain portion of the visible spectrum and reflecting the rest. In color printing, black ink is usually used instead of the combination of cyan, magenta and yellow (CMY) since it is less expensive and more accurate.

The CIE diagram can be used to conveniently quantify color purity and saturation. Saturation is determined by how much of light intensity is spread out over the spectrum. To illustrate the utility of the CIE 1931 diagram, in Figs. 1(g)–1(l) we show the relationship between spectral linewidth, color saturation, and the coordinate point location in CIE 1931 chromaticity diagram (x, y). We take Gaussian spectral distributions (which peak at 450, 525, and 650 nm, respectively) with

various spectral linewidths [achieved by varying the standard deviations ( $\sigma$ ) to simulate the additive colors (blue, green, and red),<sup>38</sup> as shown in Figs. 1(g)–1(i)]. For the reflection spectra with a single peak, the narrower linewidth indicates more saturated colors.<sup>39</sup>

The corresponding colors are mapped to the CIE 1931 diagram and plotted in Figs. 1(j)–1(l). It can be observed that when color is fully saturated, its chromaticity coordinates (x, y) locate at the outer edge of the CIE 1931 diagram. The black points in Figs. 1(j)–1(l) show the effect of increasing  $\sigma$ —the color gradually unsaturates as  $\sigma$  is increased. The central white point corresponds to a completely unsaturated color. On the other hand, the effect is the opposite for subtractive Gaussian spectra (i.e., spectra with a Gaussian dip and high reflectance elsewhere), with smaller  $\sigma$  associated with unsaturated colors and larger  $\sigma$  associated with more saturated colors. The red points inside the CIE diagram of Figs. 1(j)–1(l) show the corresponding colors formed by subtractive Gaussian spectra.

### III. STATIC PLASMONIC COLORS

Metallic nanostructures are capable of tailoring the transmission and reflection spectra by absorbing or scattering light of specific wavelengths due to the plasmonic resonance.<sup>40–51</sup> This tailoring of the spectra is accomplished in plasmonic color elements mainly by optimizing the properties of their nanostructures, namely, plasmonic nanoantennas. The optical resonances these filters support are strongly affected by the geometry, periodicity, constituent material, and ambient environment of their antennas. The overall objective of plasmonic color development is essentially focused on designing structures that give a good color performance. The optimal design process is intrinsically related to connecting their spectral responses to the incident light in the CIE diagram and the discussion in Sec. II. From the CIE diagram, one can see that there are various performance metrics that may be optimized from the saturation of color achievable to the color space available. Each antenna scheme outlined has various pros and cons; some will have highly saturated colors but a limited color space, while others will have excellent color performance, but limited transmission or reflection intensity. In this section, we consider some of the most popular designs proposed for optical elements generating static plasmonic colors and discuss their color metrics.

#### A. Gratings and periodic arrays

Metallic grating structures that disperse light of various wavelengths are great candidates for plasmonic color filters.<sup>52–66</sup> When the periodicity of a grating is smaller than the incident wavelength, the diffraction effect is avoided. Therefore, transmission or reflection that is insensitive to the incident angle may be achieved with high efficiency. By selectively converting the incident light to spatially confined modes, the transmission/reflection spectra can be tailored to generate arbitrary colors. In 2007, Cai *et al.* studied the general resonant properties of “optical metamagnetics,” which have a gap-plasmon magnetic response in the visible spectral range. These artificial materials were made of single-period arrays of paired thin silver strips as shown in Fig. 2(a).<sup>55</sup> By varying the paired-strip dimensions, the authors demonstrated gap-plasmon colors across the whole visible spectrum in both reflection and transmission regimes. As depicted in Fig. 2(b), the different strip widths generate a set of resonances in the transmission spectra for incident light with transverse magnetic (TM) polarization.

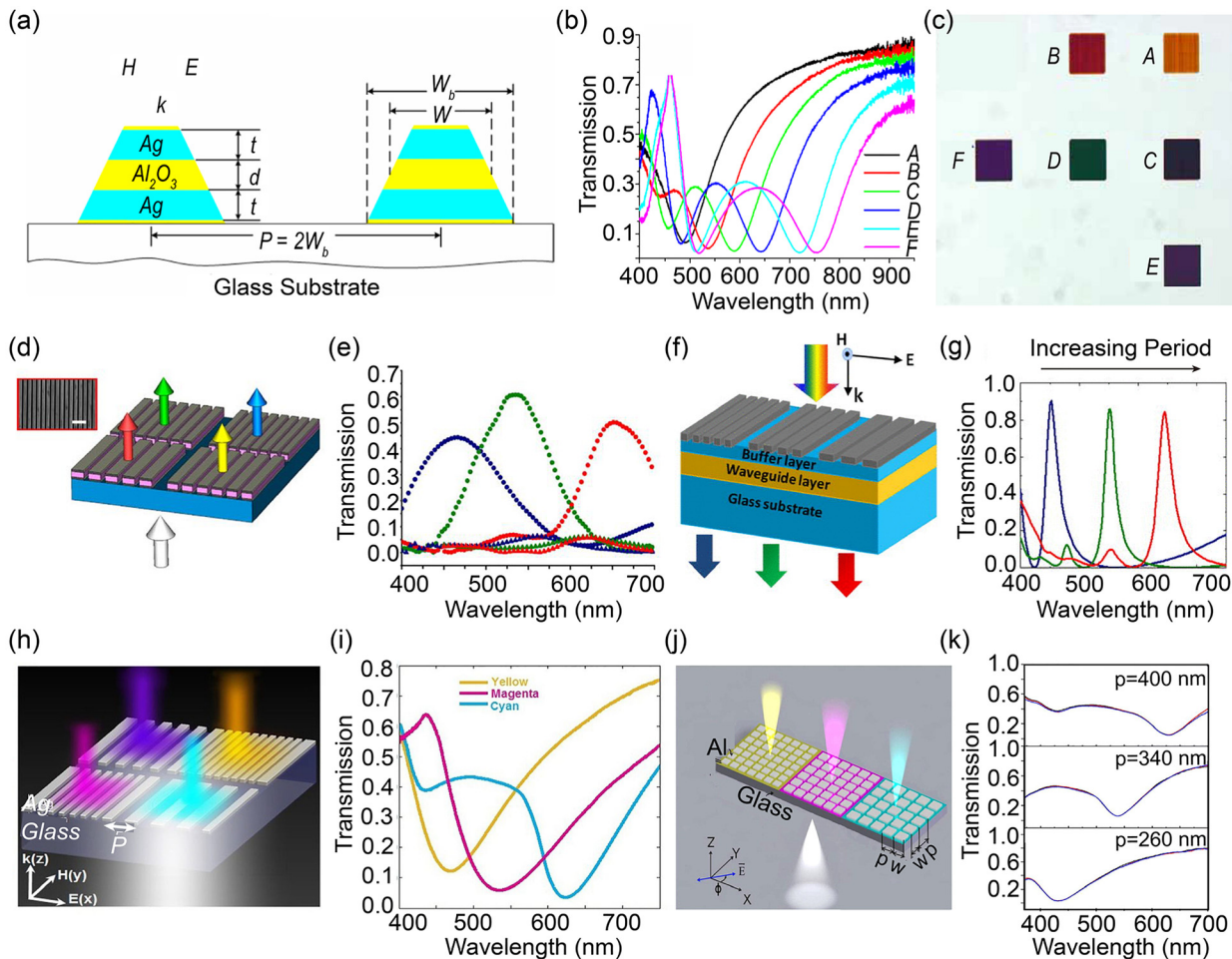


**FIG 2** a) Cross-section of an optical metamagnetic—a metal-dielectric array made of Ag nanostrips with alumina spacers. b) Transmission spectra of the optical metamagnetic samples for TM polarizations. c) Optical microscopy images of the metamagnetic samples for TM polarization. a)- c) Reproduced with permission from Cai *et al.*, Opt. Express **15** (6), 3333 (2007). Copyright 2007 Optical Society of America. d) Schematic diagram of the Al-ZnSe-Al grating color filter. Scale bar in the inset:  $1 \mu\text{m}$ . e) Measured transmission spectra of red, green, and blue for the structure in d). The electric field of the incident light is polarized perpendicular to the metallic gratings. d) and e) Reproduced with permission from Xu *et al.*, Nat. Commun. **1**, 59 (2010). Copyright 2010 Nature Publishing Group. f) Schematic of the metallic grating structure with a buffer layer and a waveguide layer. g) Simulated transmission spectra of RGB colors generated from the structure in f). f) and g) Reproduced with permission from Kaplan *et al.*, Appl. Phys. Lett. **99** (14), 143111 (2011). Copyright 2011 AIP Publishing LLC. h) Schematic diagram of the ultrathin (30 nm) Ag grating color filter with different periodicities. i) Measured transmission spectra of yellow, magenta, and cyan colors for the structure in h). The electric field of the incident light is polarized perpendicular to the metallic grating. h) and i) Reproduced with permission from Zeng *et al.*, Sci. Rep. **3**, 1 (2013). Copyright 2013 Nature Publishing Group. j) Schematic diagram of the color filter comprising a square array of Al nanopatches on a glass substrate. Incident white light is filtered into different colors, determined by the periodicity of the array. k) The measured transmission spectra of the CMY colors at normal incidence, with periodicities of 400, 340, and 260 nm, from top to bottom, for different polarization states. j) and k) Reproduced with permission from Shrestha *et al.*, Nano Lett. **14** (11), 6672 (2014). Copyright 2014 American Chemical Society.

Figure 2(c) shows microscopic color images corresponding to the transmission spectra in Fig. 2(b).

Periodic arrangements of aluminum (Al)-zinc selenide ( $\text{ZnSe}$ )-aluminum (Al) stacks on magnesium fluoride ( $\text{MgF}_2$ ) have demonstrated over 50 transmissivity around resonant wavelengths<sup>53</sup> as shown in Figs. 2(d) and 2(e). The full-width at half-maximum (FWHM) of the passband is about 100 nm, leading to saturated red, green, and blue colors. Additionally, it has also been shown that this type of plasmonic color filter could still exhibit distinct colors with only two unit cells.<sup>58</sup> Similar to Ref. 55, the color filtering effect results

from the strong magnetic response. When the incident light strikes the structure, the electric field of the light is coupled into asymmetric plasmon modes, and a major portion of the incident energy resides at the corner and edge of the Al gratings. The electric displacement current at the top and bottom Al-ZnSe interfaces forms a loop that supports the magnetic resonance.

One strategy to further enhance efficiency and color saturation is to introduce guided mode resonances.<sup>67–69</sup> Figures 2(f) and 2(g) show such an example and its performance. The structure depicted in Fig. 2(f) consists of a waveguide layer (high-index material), a buffer layer

(low-index material), and silver gratings on a glass substrate. It exhibits 90% transmission with a narrowband resonance (FWHM of 30 nm). Such outstanding performance is achieved due to constructive interference between the incident wave and the guided mode. More interestingly, the linewidth of the spectral responses [shown in Fig. 2(g)] may be tuned by adjusting the thickness of the buffer layer.<sup>67</sup>

Additive primary colors [red, green, and blue (RGB)] are usually generated by a resonant peak in the transmission/reflection spectrum, whereas subtractive colors [cyan, magenta, and yellow (CMY)] usually result from a dip in the spectrum. In 2013, a plasmonic subtractive color filtering device consisting of 30 nm-thick silver gratings on a glass substrate was presented by the Bartoli research group.<sup>62</sup> Different colors can be generated by varying the periodicity of the gratings while keeping the filling factor (FF) constant at 0.5. Figure 2(h) shows the schematic diagram of this plasmonic color filter. The transmission spectra of the yellow, magenta, and cyan color filters are presented in Fig. 2(i). The optically thin metallic layer ensures high transmission at off resonance wavelengths. The resonant dip in the transmission spectrum is obtained by hybridizing the propagating-type short-range surface plasmon polaritons (SPPs) and nonpropagating-type localized surface plasmon (LSP) modes. This resonant dip in such thin films is known as the extraordinary low transmission (ELT) effect. The transmission efficiency of ~70% at off resonance wavelength bands was achieved with parameter optimization. Additionally, the pixel size of this color filter approaches the optical diffraction limit ( $\sim \lambda/2$ ), promising useful advances in high-resolution color displays and imaging.

Besides one-dimensional metallic gratings, two dimensional plasmonic nanostructure arrays are also a popular platform for realizing highly efficient optical transmission/reflection devices.<sup>52,55,59,63–65,70</sup> For example, the Choi research group fabricated Al nanopatch arrays on glass substrates to generate subtractive colors as presented in Fig. 2(j).<sup>65</sup> If the dimensions of the nanopatches and gaps between them are optimized, this structure efficiently couples incident light to SPPs and LSPs. Such hybrid plasmon modes highly suppress transmission around the resonant wavelengths. Figure 2(k) shows that the magenta, yellow, and blue colors are generated by adjusting the periodicity of the nanopatch array. Additionally, the color-filtering effects can also be observed in reflection mode.

Additionally, the position of the resonance can be tuned by varying the FF or periodicity of the gratings. The resonance bandwidth can be decreased by introducing a waveguide layer and exploiting low-loss materials such as Ag and Al. However, surface plasmons in one-dimensional gratings can only be excited by TM waves, where the orientation of the electric field is perpendicular to the grating direction. This limitation can be alleviated by utilizing two dimensional (2D) nanostructure arrays. Aside from the example of Al nanopatches discussed, highly dense Ag nanorod arrays,<sup>52</sup> Al nanoclusters,<sup>71</sup> and plasmonic relief metasurface<sup>48,64</sup> also offer good color filtering capability.

As we have shown in Figs. 2(a) and 2(d), a certain class of plasmonic nanostructures consists of three layers—a top metallic nanostructure array layer, a dielectric spacer layer, and a bottom metallic reflector layer. Such metal-insulator-metal (MIM) structures are often referred to as gap plasmon structures because the resonant mode features confinement of the magnetic field inside the dielectric gap between metallic nanostructure and back reflector. Gap plasmon structures are good candidates for light absorption<sup>23,55,72–77</sup> and thus can be used for color generation. Benefiting from the strong near-field

coupling between the surface plasmons at the two metal-insulator interfaces, color filters based on the gap surface plasmon (GSP) mode exhibit numerous advantages: (i) subwavelength pixel size, (ii) large incident angle tolerance, (iii) sharp reflection/transmission spectrum, and (iv) a broad color palette.<sup>75,78–82</sup> These features result from the fact that the GSP mode is almost entirely confined within the MIM construction. The resonance position of GSPs can be tuned by changing the effective mode index of GSP or metallic nanostructure dimension.<sup>72</sup> For example, a configuration with periodically arranged gold nanodisks coupled to a gold substrate can be used to realize plasmonic color printing as shown in Figs. 3(a) and 3(b).<sup>79</sup> Additionally, this color filter exhibits low reliance on the surface protecting layer, allowing for device passivation with materials exhibiting excellent chemical and mechanical stability.

Al has also been used to construct GSP resonators.<sup>78</sup> Strong narrowband light absorption by individual nanoantennas facilitates the generation of saturated colors. Each single subwavelength pixel is individually tunable due to the strongly localized GSP resonance. Figures 3(c) and 3(d) show the color pixel element and tunability of the reflected color achieved by adjusting the size of the nanodisks and the periodicity.

Another slightly different GSP resonator is realized by truncating the infinitely wide dielectric spacer layer and metallic film to form “nanosandwiches,” as shown in Fig. 3(e).<sup>80</sup> Such MIM nanosandwiches can support in-phase and out-of-phase electric dipole modes due to the near-field coupling inside of the sandwich between localized plasmon modes existing at two metal-insulator interfaces. Interestingly, the enhanced in-phase dipole mode makes the resonant peak blue-shift compared to the mode in metallic nanodisk without the back reflector. This feature circumvents the limitation that short-wavelength colors (purple and blue) can only be generated by nanostructures with small dimensions. Figure 3(f) presents the experimentally obtained rainbow colors in reflection and transmission. Besides the broad color palette and clear-cut letter display, it can also be observed that even a few nanodisks can sustain vivid color performance.

## B. Subwavelength nanohole array

2D grating nanostructures can produce a resonant peak or dip in the transmission/reflection spectrum by excitation of SPP, LSPR, or their combination. According to Babinet’s principle,<sup>83</sup> subwavelength nanohole arrays exhibit similar optical responses to their complementary structure nanodisk or nanopatch arrays.<sup>84–94</sup> The coupling of incident light to surface plasmons leads to the unusual zero-order transmission and is termed extraordinary optical transmission (EOT).<sup>22,95,96</sup> EOT is caused by the interference of SPPs between adjacent nanoholes that selectively enhances the transmission at the resonant wavelength. Employing this effect, a broad palette of colors can be rendered by adjusting the period of the nanohole array. This possibility is illustrated by Eqs. (1) (for square nanohole arrays) and (2) (for triangular nanohole arrays),<sup>27</sup>

$$\lambda = \frac{p}{\sqrt{i^2 + j^2}} \sqrt{\frac{\epsilon_m \epsilon_d}{\epsilon_m + \epsilon_d}}, \quad (1)$$

$$\lambda = \frac{\sqrt{3}}{2} \frac{p}{\sqrt{(i^2 + j^2) - ij}} \sqrt{\frac{\epsilon_m \epsilon_d}{\epsilon_m + \epsilon_d}}, \quad (2)$$

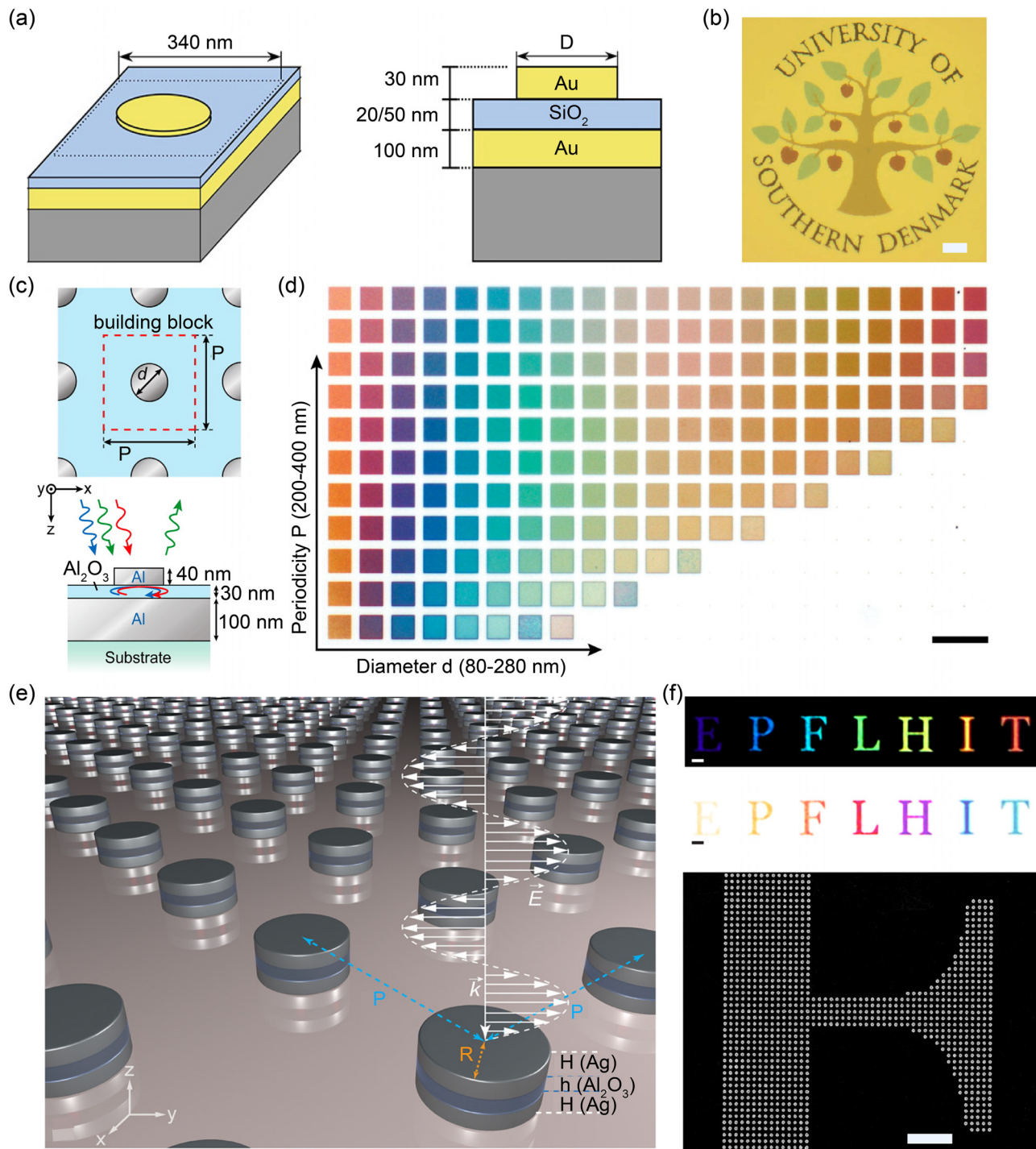


**FIG 3** a) Schematic diagram of Au disk supported by a continuous  $\text{SiO}_2$  layer stacked on an Au back-reflector. b) Color display of the logo of the University of Southern Denmark. Scale bar: 10  $\mu\text{m}$ . a) and b) Reproduced with permission from Roberts *et al.*, *Nano Lett.* **14** (2), 783 (2014). Copyright 2014 American Chemical Society. c) Schematic of the top view (top) and the cross-sectional view (bottom) of Al nanodisks placed on an  $\text{Al}_2\text{O}_3$ -coated Al film. d) Optical microscopy images of the nanodisk arrays with diameter  $d$  varying from 80 to 280 nm with an increasing step of 10 nm and periodicity  $P$  varying from 200 to 400 nm with an increasing step of 20 nm. Scale bar: 25  $\mu\text{m}$ . c) and d) Reproduced with permission from Miyata *et al.*, *Nano Lett.* **16** (5), 3166 (2016). Copyright 2016 American Chemical Society. e) Schematic diagram of the  $\text{Ag}-\text{Al}_2\text{O}_3-\text{Ag}$  nanodisk arrays residing on a glass substrate. f) Experimental reflection (upper panel) and transmission (middle panel) color displays, and SEM of the central part of the letter "E" (lower panel). Scale bar: 2  $\mu\text{m}$ . e) and f) Reproduced with permission from Wang *et al.*, *Nano Lett.* **17**, 5 (2017). Copyright 2017 American Chemical Society.

where  $\lambda$  is the resonant wavelength,  $p$  is the periodicity of the array,  $\varepsilon_m$  and  $\varepsilon_d$  are the permittivities of the metal and the dielectric materials, respectively, and  $i$  and  $j$  are the scattering orders of the array.

Recently, a polarization-independent, EOT-based, subtractive color filter composed of a periodically perforated silver film was proposed.<sup>84–86</sup> The authors systematically investigated the relationship between the generated colors and the geometric parameters of the nanoholes. Sun *et al.* found that the color filtering properties are strongly related to the thickness of the film and periodicity of the nanohole array through the short-range SPP modes.<sup>85</sup> The color saturation can be increased by adjusting the shape of the lattice (how the nanoholes are arranged) to hexagon

or square.<sup>86</sup> Typical experimental results of the theoretically optimized color filters are presented in Fig. 4(a).

To improve the color quality, e.g., saturation and hue, the Yang research group combined the periodically perforated silver film with a silver reflector to realize perfect light absorption.<sup>84</sup> The structure and two plasmonic color images are shown in Fig. 4(b).

Compared with Ag, Al has a higher plasma frequency which leads to lower optical losses in the wavelength range of 400–500 nm.<sup>93</sup> This feature makes Al nanohole arrays specifically suitable for generating vibrant blue colors. The color palette can be further expanded by altering the periodicity, nanohole geometry, and the shape of the lattice as presented in Fig. 4(c).<sup>93</sup> Aside from the Al-SiO<sub>2</sub> and Al-SiO<sub>2</sub>-Al

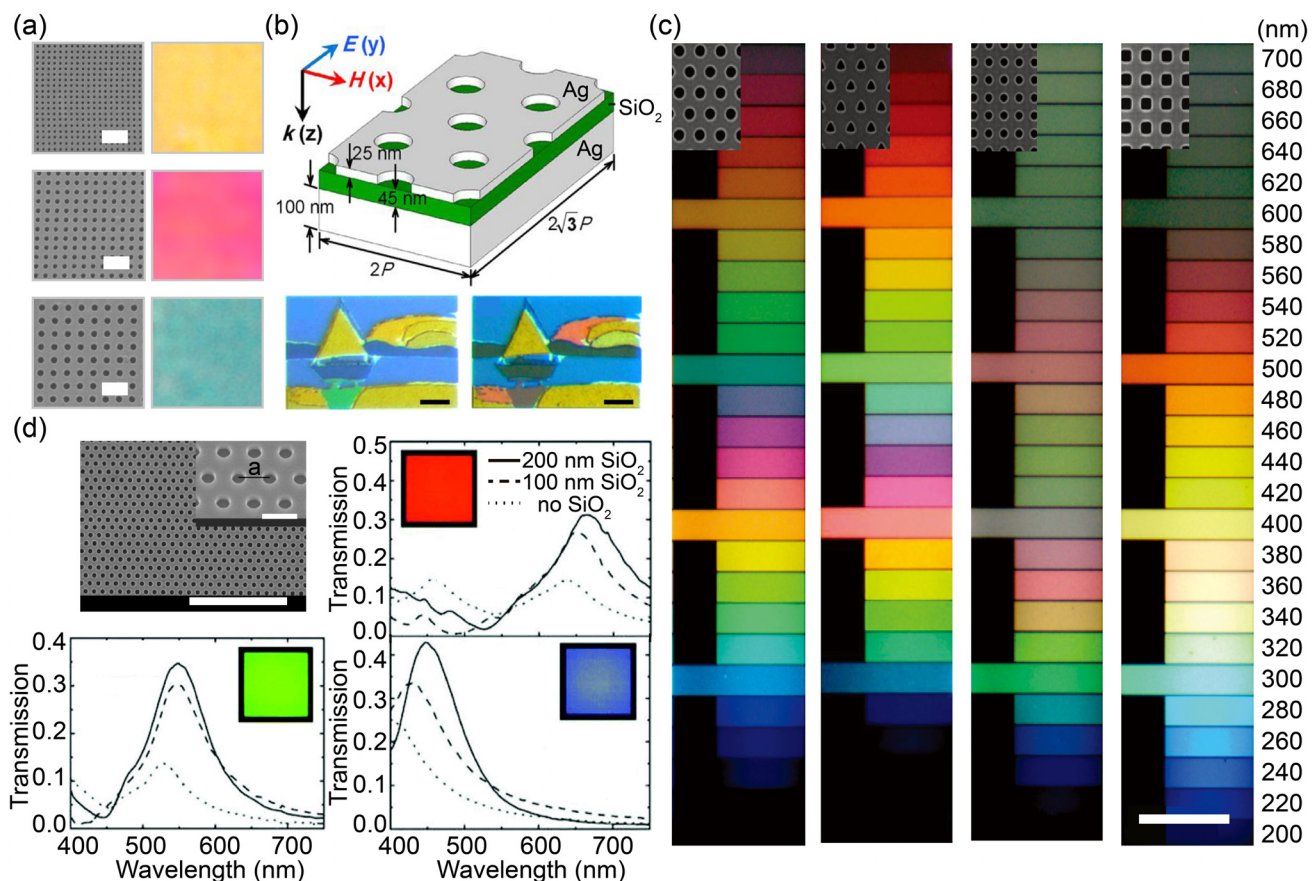


**FIG 4** a) Left) The SEM images of periodically perforated Ag film with three select periods of 140 nm, 230 nm, and 320 nm, from top to bottom. Scale bars: 500 nm. Right) The optical micrographs under white light normal illumination. Reproduced with permission from Sun *et al.*, Opt. Commun. **333**, 16 (2014). Copyright 2014 Elsevier. b) A nanohole array arranged in a triangular lattice and an Ag reflector separated by a SiO<sub>2</sub> layer, shown schematically at the top left. Different colors are realized by varying the periodicity and the hole radius, as well as by applying a protective polymethyl methacrylate (PMMA) coating, as illustrated in the pastel painting at the bottom left (without PMMA) and right (with PMMA). Scale bars: 10  $\mu\text{m}$ , electric field;  $H$ , magnetic field;  $k$ , incident light wave vector). Reproduced with permission from Cheng *et al.*, Sci. Rep. **5**, 1 (2015). Copyright 2015 Nature Publishing Group. c) From left to right, optical microscope images of Al nanohole arrays with circular holes in hexagonal lattice, triangular holes in a hexagonal lattice, circular holes in a square array, and square holes in a square array. Colors are tuned by varying the periodicity and the shape of nanohole and lattice. Reproduced with permission from Inoue *et al.*, Appl. Phys. Lett. **98** (9), 93113 (2011). Copyright 2011 AIP Publishing. Scale bar: 100  $\mu\text{m}$ . d) SEM of the Al nanohole array and the measured transmission spectra of three primary color filters: a red filter hole array with  $a = 430$  nm (top right), a green filter hole array with  $a = 330$  nm (bottom left), a blue filter hole array with  $a = 250$  nm (bottom right). The color filters are measured with no SiO<sub>2</sub> capping layer, with a 100 nm-thick SiO<sub>2</sub> capping layer, and with a 200 nm-thick SiO<sub>2</sub> capping layer, which are marked as a dotted line, dashed line, and solid line, respectively. The insets are optical micrographs of a square patch consisting of each nanohole array with a 200 nm-thick SiO<sub>2</sub> capping layer. Scale bar: 5  $\mu\text{m}$ , scale bar inset: 500 nm. d) Reproduced with permission from Chen and Cumming, Opt. Express **18** (13), 14056 (2010). Copyright 2010 Optical Society of America.

configurations, Chen *et al.* deposited a  $\text{SiO}_2$  layer on both sides of the perforated Al film.<sup>90</sup> As a result, the two-surface plasmon modes on both Al- $\text{SiO}_2$  interfaces resonate at the same wavelength, thereby increasing transmission. Figure 4(d) shows that this configuration substantially enhances the color saturation and the transmission efficiency in comparison with the metallic nanostructures without  $\text{SiO}_2$  capping layers.

### C. Hybridized nanohole and nanodisk arrays

Periodic nanohole arrays realize the color filtering effect via EOT. Multiple elementary structures are required to cause the interference of SPPs between neighboring elements, leading to large pixel sizes in color displays. Alternatively, periodic or isolated metallic nanodisks can generate colors by excitation of LSPR; thus the pixel size can be diminished to wavelength scales. Interestingly, the near-field interaction of nanodisks and nanoholes offers the

possibility to produce a pixel smaller than half-wavelength. By placing an Au-Ag nanodisk array above a holey back-reflector, the Yang research group experimentally realized 250 nm-pitched pixels that reflect individual colors, increasing the spatial resolution to  $\sim 100\,000$  dpi.<sup>26</sup> Figures 5(a) and 5(b) show the representative nanostructure and the color palette achieved with different gaps and disk sizes. It can be observed that a broad range of colors is generated even with a constant periodicity. In Fig. 5(c), an image of Lena<sup>97</sup> is produced by nanostructures with a periodicity of 125 nm and different disk radii. One pixel in this image is composed of  $2 \times 2$  nanodisks. Such a small pixel size (250 nm) approaches the theoretical diffraction limit of optical microscopy. Figure 5(d) shows a checkerboard pattern with alternating colors. Each square in the checkerboard is composed of a  $2 \times 2$  array of nanodisks. This resolution test illustrates that such small pixels are indeed able to present distinguishable colors.

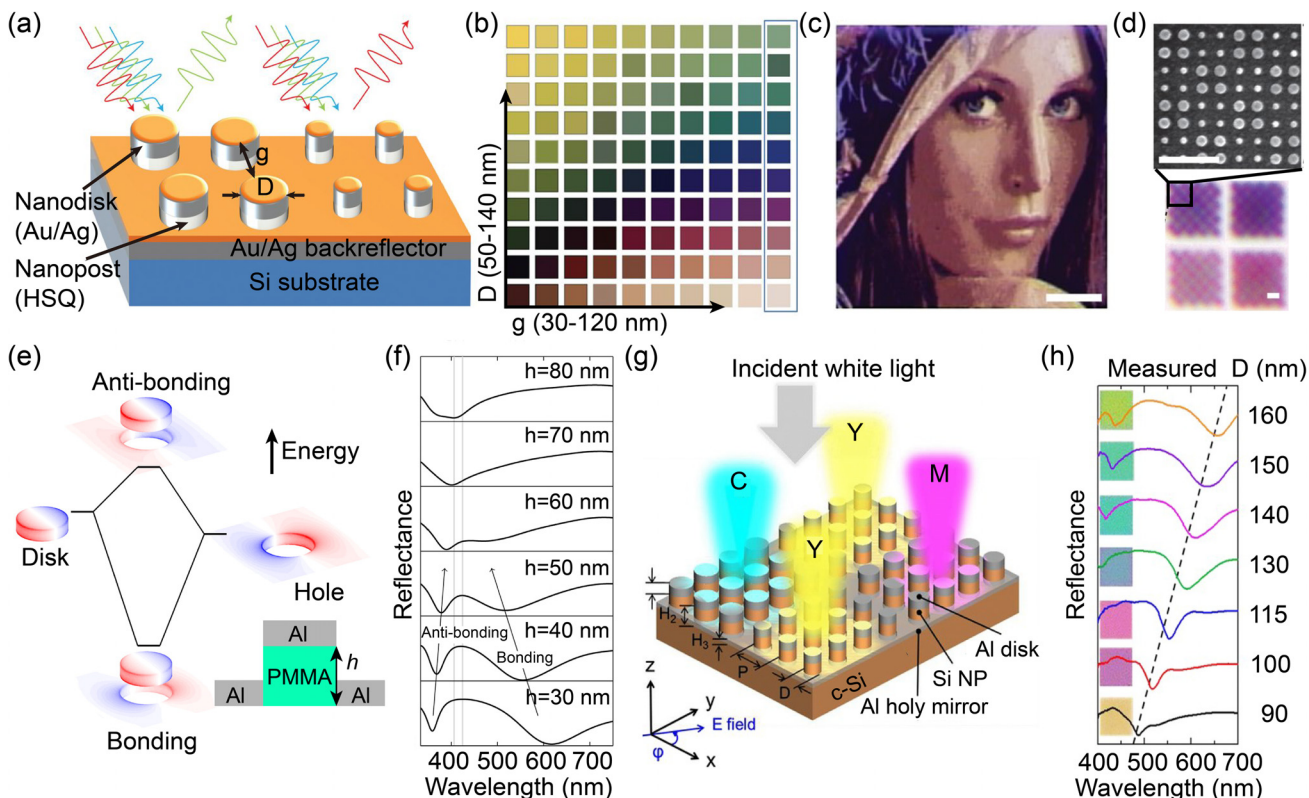


**FIG 5** a) Schematic diagram of plasmonic color filters composed of Au/Ag nanodisks array against a back reflector. b) Color palette achieved by varying the disk diameter D from 50 to 140 nm and gap size g from 30 to 120 nm. c) Optical micrographs of the Lena image. Scale bar: 1  $\mu\text{m}$ . d) Checkerboard pattern with color squares of 250 nm consisting of  $2 \times 2$  nanodisks, as shown in the SEM. Scale bar: 500 nm. a)- d) Reproduced with permission from Kumar *et al.*, Nat. Nanotechnol. 7 (9), 557 (2012). Copyright 2012 Nature Publishing Group. e) The hybridized plasmon modes of the disk-hole construction produce two new modes: a low energy bonding mode and a high energy anti-bonding mode. The inset presents the cross section of the unit-cell structure, with  $h$  representing the height of the dielectric pillar. f) Reflectance spectra when varying  $h$ . The two new modes can be observed as resonant dips in the spectra, implying that the coupling decreases with increasing pillar height. e) and f) Reproduced with permission from Clausen *et al.*, Nano Lett. 14 (8), 4499 (2014). Copyright 2014 American Chemical Society. g) Schematic diagram of subtractive color filter comprised of c-Si pillars integrated with an Al hole-disk construction. Three primary subtractive colors can be produced in response to normally incident white light. P is the periodicity and D is the diameter of the pillars.  $H_1$ ,  $H_2$ , and  $H_3$  indicate the thicknesses of Al disks, Si pillars, and Al holey film, respectively. h) The reflection spectra of the proposed color filters of which the diameter D ranges from 90 to 160 nm with a constant periodicity of  $P = 240$  nm. The location of the reflection dips are traced by the dashed line. The insets present the optical microscopic images of the color filters with a footprint of  $30 \mu\text{m} \times 30 \mu\text{m}$ . g) and h) Reproduced with permission from Yue *et al.*, Laser Photonics Rev. 11 (3), 1600285 (2017). Copyright 2017 John Wiley and Sons.

In the previous configuration, the top metallic nanodisks support LSPR, and the nanohole back-reflector is, in essence, a Babinet complementary screen.<sup>98</sup> The plasmon dipole mode excited in the nanohole hybridizes with the localized plasmon mode confined in the lifted nanodisk. Besides the Au-Ag pair used in the reference,<sup>26</sup> Al is also investigated in these hole-disk coupling constructions.<sup>59,81,82,99</sup> As shown in Fig. 5(e), both the Al nanodisks and nanoholes perforated in the Al film support dipolar resonances, increasing optical absorption at specific wavelengths. When the nanodisk is close to the nanohole, the two modes hybridize into two new modes: a “bonding” mode and an “antibonding” mode.<sup>82</sup> The bonding (antibonding) mode is characterized by the out-of-phase (in-phase) charge oscillations in the nanodisk and nanohole. Figure 5(f) indicates that the height of the dielectric pillars determines the coupling strength between them. Each of the two new modes results in significant resonant dips in the reflection spectra, resulting in vibrant colors.

Højlund-Nielsen and co-authors demonstrated possible routes for mass-production of plasmonic colors based on aluminum nanostructures<sup>82</sup> by using polymer replication techniques (roll-to-roll printing, film insert molding, and direct injection molding of polymeric materials).<sup>100</sup>

When the commonly used hydrogen silsesquioxane (HSQ) pillars are replaced with crystalline silicon (c-Si) pillars, a magnetic dipole mode is resonantly excited in the c-Si via Mie scattering.<sup>99</sup> Additionally, this mode can be efficiently coupled to the Si substrate, producing a pronounced resonant dip in the reflection spectrum. The resonance position of the reflection dip can be adjusted across the visible spectrum by changing the diameter of the Si pillar. The Al disk mirror and holey mirror are of great importance in this construction since they enhance the reflectance and confine the magnetic dipole mode inside the Si pillar. Figure 5(g) schematically shows this color filter structure, and the achieved large color gamut is presented in Fig. 5(h).

#### IV. DYNAMICALLY TUNABLE PLASMONIC COLORS

Color filters enabled by metallic subwavelength nanostructures exhibit a number of advantages such as high spatial resolution, long-term durability, environmental friendliness, and scalable manufacturability.<sup>28</sup> Since the resonant frequency of plasmonic color systems depends on the resonators’ geometry and composition, most plasmonic color filters can only generate static colors because the geometry and material of the nanostructures are unchangeable. However, the rapid development of color display and data storage technologies calls for dynamically tunable color filters.<sup>29</sup> For data storage, in particular, it is highly desirable to encode numerous color states into a single pixel and retrieve them with high fidelity. In this section, we review the recent efforts toward realizing this goal.

##### A. Polarization tuning

The most straightforward approach to dynamically tunable colors is to map the polarization states of the incident white light to different colors.<sup>39,101–106</sup> This polarization-dependent color filtering effect is of great importance in numerous applications. First, it provides a degree of freedom to manipulate the plasmon resonance mode, so that data storage capacity can be increased in a color-based information storage system.<sup>107,108</sup> Second, it can be used in the birefringent screening of skin cancer tissue.<sup>101,109</sup> Third, it enables three-

dimensional (3D) stereoscopic color prints<sup>105</sup> and encryption of messages that can be only decrypted by having the correct “polarization keys.”<sup>104</sup>

In 2012, subwavelength cross-shaped nanoantennas with uneven arm lengths were proposed and termed chromatic plasmonic polarizers (CPPs), as shown in Fig. 6(a).<sup>101</sup> The LSPR wavelength is determined by the arm length along the incident polarization direction; therefore, the cross-shaped nanoantennas support two independently tunable LSPRs. As a result, linearly polarized (LP) incident white light is split into two different colors that can be selectively generated depending on the polarization state of the incident light. Figure 6(b) indicates that the polarization-dependent color palette of such a CPP can be mapped to a continuous line in the CIE diagram. Babinet effect allows for CPPs to be realized as cross-shaped aperture arrays.<sup>102–104</sup> Figure 6(c) schematically shows an isolated cross-shaped aperture in an Al film. When changing the polarization of the incident white light, dual-color selectivity in one nanopixel is realized. Furthermore, the color palette can be enriched by varying the dimensions of the aperture.<sup>102</sup> Consequently, images that display switchable color schemes at different polarization states can be created as shown in Fig. 6(d).

Besides cross-shaped nanoantennas, pixels consisting of Al elliptical nanodisks or coupled nanosquare dimers can also exhibit polarization-dependent color filtering effect as shown in Fig. 6(e).<sup>105</sup> Colors generated from the elliptical nanodisk array are dominated by the length of the ellipse axis parallel to the incident polarization. However, the color intended for one polarization can still be observed in the orthogonal polarization. This drawback is called the “cross talk” effect, which leads to the undesired mixing of the two color states of the pixel. In order to solve this problem, Goh *et al.* exploited an elementary structure consisting of two coupled Al nanosquare dimers. In this case, a strong field is confined in the dimer’s gap, and a coupled dipole mode is excited in one polarization, with coupling intensity determined by the gap size. When the incident polarization is rotated by 90°, plasmon coupling disappears; therefore, the gap size does not influence the color performance. As a result, the cross talk effect is effectively reduced.<sup>105</sup> Figure 6(f) shows the comparison between the microprints composed of elliptical nanodisks and coupled nanosquare dimers when illuminated under orthogonal polarizations.

Polarization of the incident light not only acts as a degree of freedom to control the output colors but can also be manipulated to increase the color purity. In 2018, Song *et al.* proposed a shallow plasmonic grating (SPG) to achieve high-purity full-color generation based on photon spin restoration effect, as shown in Fig. 6(g).<sup>39</sup> It is well known that the polarization helicity is reversed when circularly polarized (CP) light is reflected from a common mirror. However, this SPG design can selectively reflect a CP light to its copolarized state at specific wavelengths determined by the periodicity of the grating. Figure 6(h) shows the experimentally measured reflection spectra of red, green, and blue colors with three corresponding photographed images of the sample. Since both SPP and LSP contribute collectively to induce the 180° phase difference between the two orthogonal linear polarization components (*x* and *y* polarizations), ultranarrowband resonance with a FWHM of 16 nm and high reflectance (~75%) is experimentally realized. Additionally, large-area polarization-dependent colors offer great potential for the applications of optical data encryption [Fig. 6(i)] and storage, as well as sensing with a chromatic response observable to the naked eye.

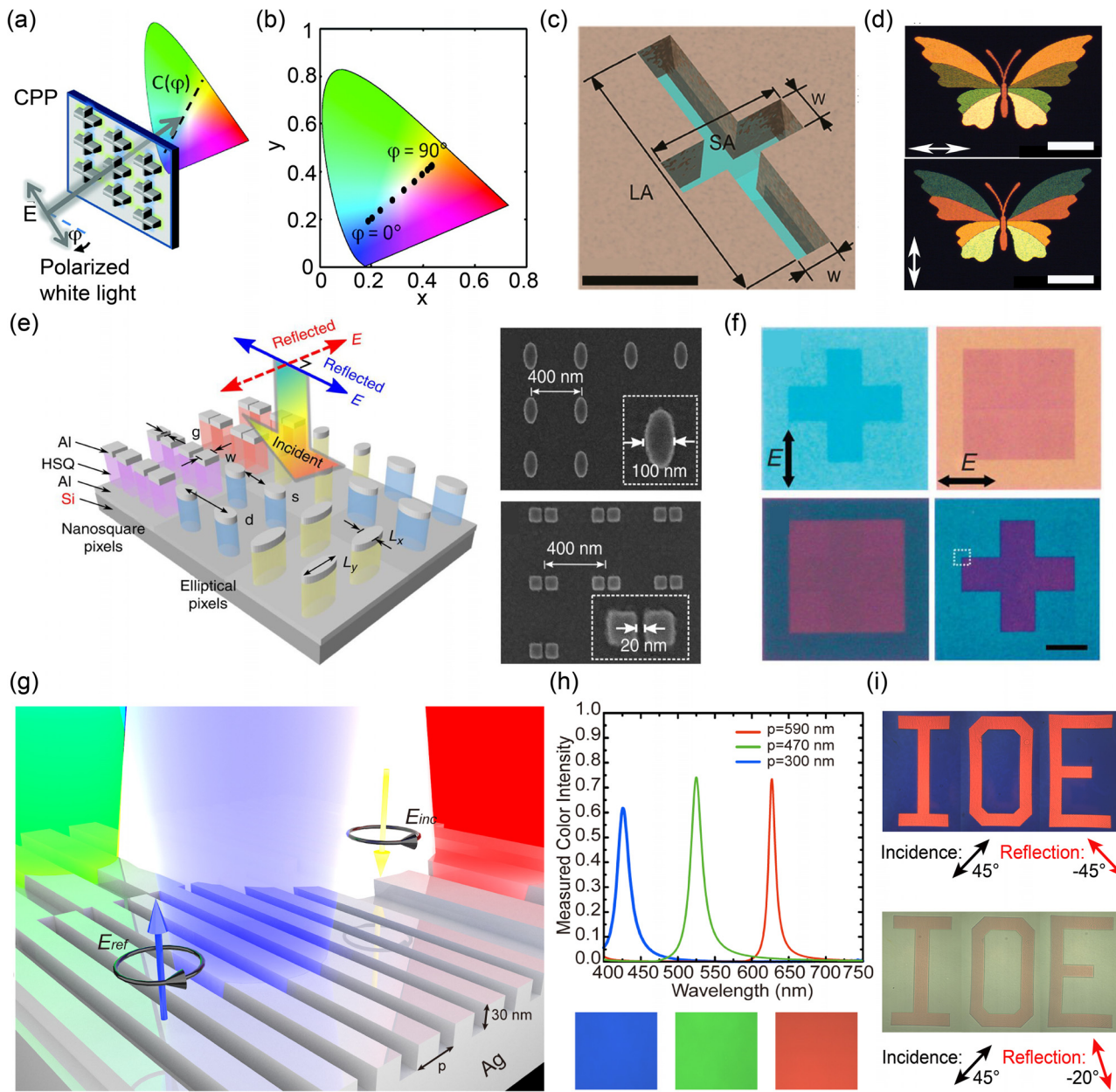


**FIG 6** a) Schematic diagram of the chromatic plasmonic polarizer (CPP) operation concept. CPP consists of cross-shaped nanoantennas, which map the incident white light with different linear polarization angles to different colors via LSPR. b) Color palette of the CPP on the CIE 1931 chromaticity diagram. a) and b) Reproduced with permission from Ellenbogen *et al.*, *Nano Lett.* **12** (2), 1026 (2012). Copyright 2012 American Chemical Society. c) Schematic of one cross-shaped aperture, with its dimensions  $LA = 203$  nm,  $SA = 120$  nm,  $P = 340$  nm, and  $w = 30$  nm. Scale bar: 100 nm. d) Microscopic images of a butterfly with switchable colors under different incident polarization states. The black arrows indicate the incident polarization direction. Scale bar: 40  $\mu\text{m}$ . c) and d) Reproduced with permission from Li *et al.*, *ACS Nano* **10** (1), 492 (2016). Copyright 2016 American Chemical Society. e) Schematic diagram of the elliptical nanodisks and coupled nanosquare dimmers. Various colors are encoded into the  $L_x$  and  $L_y$  of the elliptical nanodisks, and  $w$  and  $g$  for coupled nanosquare dimers. The insets are SEM of the nanoellipses (top) and coupled nanosquares dimers (bottom). f) Optical microprints of a square and a cross patterned into the same area illuminated under  $x$  and  $y$  polarized light. The patterns are formed from elliptical nanodisk arrays (top) and coupled nanosquare dimers (bottom). Scale bar: 20  $\mu\text{m}$ . e) and f) Reproduced with permission from Goh *et al.*, *Nat. Commun.* **5**, 5361 (2014). Copyright 2014 Nature Publishing Group. g) Schematic diagram of the plasmonic shallow grating (PSG) interaction. Yellow and blue arrows indicate the incident and reflected right-handed circularly polarized (CP) light. Black arrows depict the helicity of the incident and reflected waves. Red, green, and blue beams represent the reflected waves with restored helicity. The filling factor of the grating is fixed to be 0.55. h) Experimental reflection spectra when illuminated by 45° polarized light at normal incidence. The three insets are photographed images of the sample corresponding to the red, green, and blue spectrum. i) Microscopic images "IOE" of the sample for 45° polarized incident light. The polarization direction of the reflected light is  $-45^\circ$  (top) and  $-20^\circ$  (bottom). g)–i) Reproduced with permission from Song *et al.*, *Nanophotonics* **7** (1), 323 (2018). Copyright 2018 DE GRUYTER.

## B. Electrical tuning

Electrically tunable plasmonic metasurfaces can lead to a breakthrough in controllable light manipulation at ultracompact scales. By selectively controlling the optical absorption of such structures with an electrical bias, one can use such metasurfaces for dynamic color generation. This feature can be realized by changing various parameters, four of which are discussed here: the orientation of the resonant element, the incident light polarization, the dielectric spacer properties, and the geometry of the nanostructure.<sup>110–119</sup>

The orientation of the resonant element can be changed with the help of electrical bias. Depending on the incident light polarization, such oriented elements interact with light to give distinct optical responses. Nair *et al.* demonstrated electrically tunable colors by

changing the orientation of bent-core and rod-shaped structures.<sup>114</sup>

Applying different biases to change the alignment of helicoidal cholesteric molecules results in different color rendition.<sup>117</sup> Figure 7(a) shows field-induced behavior and resulting colors from cholesteric molecules. As with standard liquid crystal devices, this kind of devices needs constant power to hold the nanostructure orientation using a static electric field; therefore, it would consume energy to hold a state. Dynamic tuning of pixels by changing the orientation of gold nanorods has been utilized in the 7 segment numerical indicator.<sup>120</sup>

In 2017, Lee *et al.* demonstrated a polarization modulation mechanism by using a twisted-nematic liquid crystal. In this method, a broad palette of colors can be generated with a spectral tuning range of 120 nm.<sup>116</sup> Figure 7(b) shows how biasing such a polarization

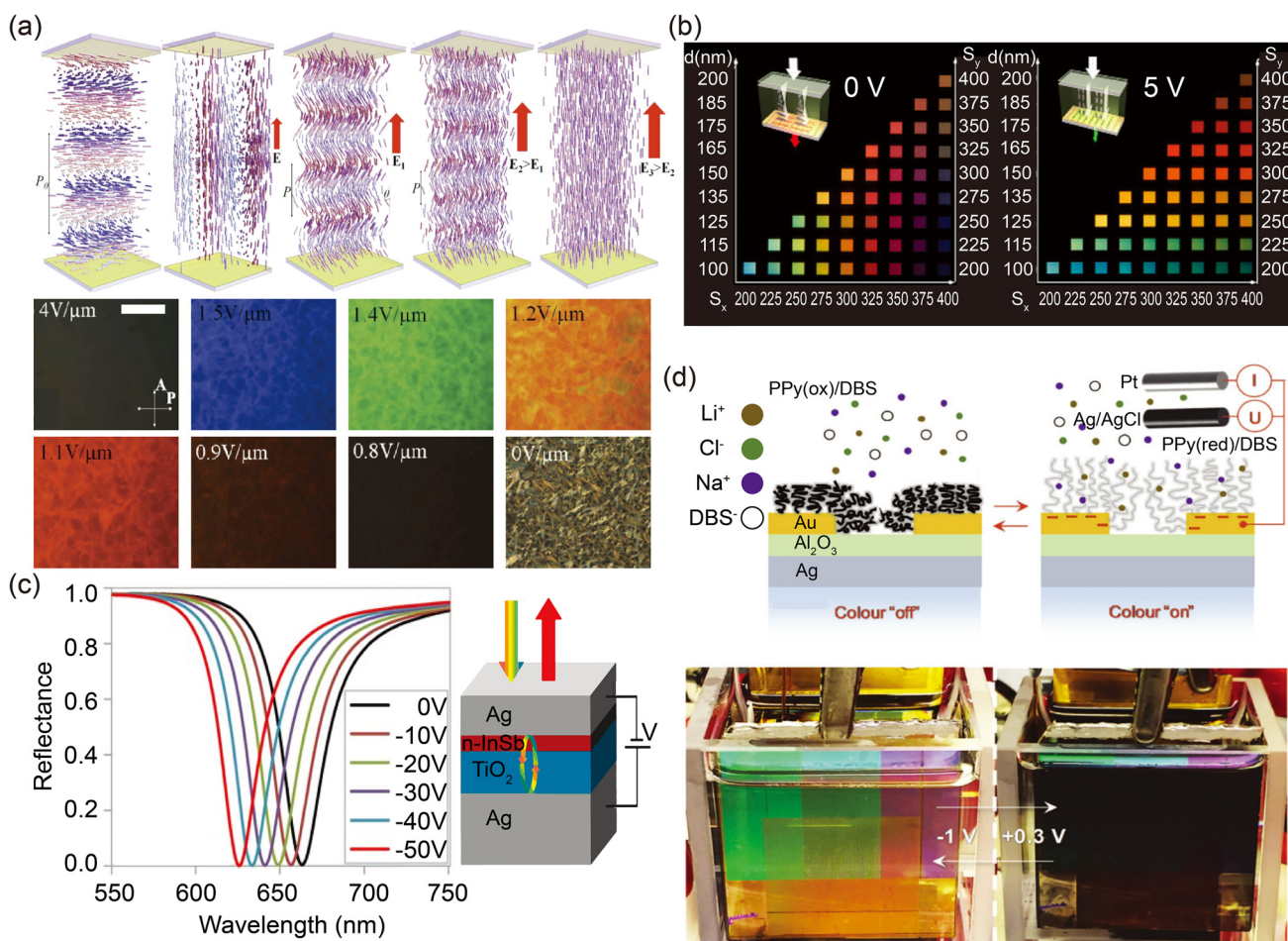


**FIG 7** Electrical color tuning by changing a) the orientation of the resonant element: Field induced behavior and resulting colors from cholesteric molecules. The eight insets show the various colors at different biasing voltages. a) Reproduced with permission from Xiang *et al.*, *Adv. Mater.* **27** (19), 3014–2015. Copyright 2015 John Wiley and Sons. b) Incident polarization: Electrical-bias driven polarization control for color switching. Charts show optical photograph at 0 V and 5 V biases. Insets show the schematic of biasing scheme. b) Reproduced with permission from Lee *et al.*, *ACS Photonics* **4** (8), 1954–2017. Copyright 2017 American Chemical Society. c) Property or shape of the dielectric spacer: Numerical demonstration of changing reflectivity with modulation of optical property in n-InSb layer. c) Reproduced with permission from Mirshafeyan and Gregory, *Sci. Rep.* **8** (1), 2635–2017. Copyright 2017 Nature Publishing Group. d) Shape of the resonant element: Modulation with polymerization on Au nanoholes. Top figures show the “on” state and “off” state polymerization. Bottom figures show the photographs of the color sheet at -1 V and 0.3 V biases. d) Reproduced with permission from Xiong *et al.*, *Adv. Mater.* **28** (45), 9956–2016. Copyright 2016 John Wiley and Sons.

modulator can change the color from a simple periodic hole array structure with different periodicities along the  $x$ - and  $y$ -axes. The polarization response of the structure limits such devices' operation speed. Additionally, the liquid-crystal-based polarization controller also requires constant power to hold the state of polarization.

It has been shown that the refractive index of transparent conducting oxides (TCOs) can be changed in the visible region by electrical biasing.<sup>112</sup> Mirshafieyan and Gregory showed that the resonant peak in the reflection spectrum can be shifted by biasing and changing the optical property of n-doped indium antimonide (n-InSb) sandwiched between Ag layers. Therefore, they numerically show that the output color can be dynamically tuned [Fig. 7(c)].<sup>115</sup> Such a device for color filtering is yet to be demonstrated experimentally but has the potential to be more robust and reliable than liquid-crystal-based tunable color filters as it does not have any liquid phase part.

The shape of the resonant element can be effectively changed with the help of conducting polymers. This changing of shape can effectively dampen the plasmon resonance, giving rise to plasmonic colors. Xiong *et al.* showed plasmonic metasurface consisting of an Au nanohole array, Al<sub>2</sub>O<sub>3</sub> spacer, and Ag thin film mirror.<sup>110</sup> When the thickness of the dielectric spacer is varied, red, green, and blue colors can be generated in the reflection mode. To obtain tunable colors, they employed conjugated polymer films. By biasing a solution containing sodium dodecylbenzenesulfonate (NaDBS) and pyrrole, they could selectively change the shape of the conductive polymer; thus, through dampening or strengthening plasmon resonance, the device can selectively display color. Figure 7(d) shows the mechanism of dampening plasmonic resonance and switching the colors at the off and on states. By dynamically controlling deposition of silver on predefined hollow shells, similar electrical switching between "colored" and "bleached" state is demonstrated.<sup>121</sup> Such displays can have smaller switching power than e-ink and liquid crystal display (LCD).

Similar to electrical tuning, magnetic color tuning can be achieved through changing the orientation of plasmonic nanoparticles with an external magnetic field. A plasmonic-magnetic nanocomposite can be rotated with the external magnetic field to display colors selectively. Thus, colloidal nanostructures of Au-nanorod hybrids<sup>122</sup> and Fe<sub>2</sub>O<sub>3</sub> nanorods embedded in a gold shell<sup>123,124</sup> have been used to demonstrate tuning of extinction coefficient, and therefore to actively change the color through magnetic field manipulation.

### C. Temperature tuning and laser-induced plasmonic coloration

Temperature can cause modification to material's optical properties and morphology and has been employed as a tuning mechanism for plasmonic color displays. Drastic temperature-induced refractive index change in vanadium dioxide (VO<sub>2</sub>)—which happens at a relatively low insulator-metal transition temperature ( $\sim 66^\circ\text{C}$ )—has attracted tremendous research attention lately.<sup>125–127</sup> This behavior opens up an avenue for dynamic plasmonic color tuning by changing temperature and is realized in Ref. 128, where the authors pattern Ag nanodisks on a SiO<sub>2</sub>/VO<sub>2</sub> double layer [Fig. 8(a)] to form a reflection-type metasurface. The reflection spectrum is largely governed by the LSPR on the Ag nanodisks; vibrant colors can be generated when the disk diameter and interdisk distance are varied. Since the LSPR is highly sensitive to the refractive index of the environment surrounding the Ag nanodisks, the reflection spectrum is altered when the VO<sub>2</sub>

insulator-to-metal transition is induced at elevated temperature, leading to a change in the reflected color. In Fig. 8(b), the authors showcase such color tuning enabled by temperature change. One intriguing property of VO<sub>2</sub> is the reversibility of the temperature-induced phase transition. Thus, the plasmonic colors from the Ag disk-VO<sub>2</sub> hybrid structure are recovered once the device cools below the transition temperature. Also, the temperature-induced dielectric-metallic transition in germanium antimony telluride (Ge<sub>2</sub>Sb<sub>2</sub>:Te<sub>5</sub> or GST) has been harnessed as a mechanism to tune the reflected and transmitted colors from GST grating structures.<sup>129</sup> Another class of temperature-controlled plasmonic color device is enabled by a temperature-induced modification of material morphology. Yu *et al.* used rapid thermal annealing ( $750^\circ\text{C}$ , 90 s) of silver films for color tuning.<sup>130</sup> They show that by simply tuning the size and contact angle of the dewetted metallic nanoparticles, one can achieve narrow resonances and large tunability in the visible spectral range. However, this approach is limited to inducing uniform color changes on a whole substrate. In order to obtain local color changes, one could utilize laser irradiation. In a work by Wang *et al.*,<sup>77</sup> the laser heating of plasmonic structures is carefully studied in both the spatial and temporal domains.

Chen *et al.* show in a meticulously conducted research that nano-patterned Au hexahedrons undergo different shape and crystallinity changes when they are subject to laser irradiation of different intensities, as shown in Fig. 8(c).<sup>131</sup> Such findings imply that the spectrum of plasmonic nanoparticles can be controlled by laser intensity because the LSPR is very sensitive to the geometry of the nanoparticles [Fig. 8(d)]. Zhu *et al.* utilized this idea to design a device for plasmonic color printing, where a metasurface is used as a "paper," and a tightly focused pulsed laser beam works as the "inkjet head."<sup>132</sup> In this work, a uniform metasurface is fabricated by depositing Al on polymer nanopillars to form Al nanodisks, and the pulsed laser directly "writes" on the metasurface to change the morphology of the affected Al nanodisks by heating them beyond their melting point. As mentioned before, the shape of the Al nanodisks, thereby the reflection spectrum, can be controlled by the laser pulse energy, enabling vivid color display as shown in Fig. 8(e). The authors also achieve subdiffraction-limit spatial resolution by manipulating the laser intensity close to the Al nanodisk melting threshold, so that a single nanodisk (with subdiffraction size) is melted by each laser pulse to form an image pixel. As a result, a resolution of 127 000 dpi is achievable with this technique [Fig. 8(f)]. In Ref. 133, the same group uses a spatial light modulator, instead of raster scanning, in order to realize high throughput holographic resonant laser printing. This approach could enable on-demand mass-production of customized metasurfaces for color printing and other applications. A natural extension of the work by Zhu *et al.*<sup>132</sup> was recently presented by Zhang *et al.*, where the paper has a form of a gap plasmon type metasurfaces with aluminum cross-type nanostructures fabricated on the aluminum mirror with a silica spacer.<sup>134</sup> The authors use the anisotropic thermoplasmonic shape transition of the Al cross nanostructures. In this case, the metasurfaces are illuminated with linearly polarized femtosecond laser radiation, and the light is polarized along one of the cross arms. The laser pulses induce heating and reshaping of one of the cross arms and result in the tuning of the structure reflection (and absorption) at light polarization that is the same as the modifying laser, while the reflection measured with cross-polarized linear light is nearly unaffected. An earlier

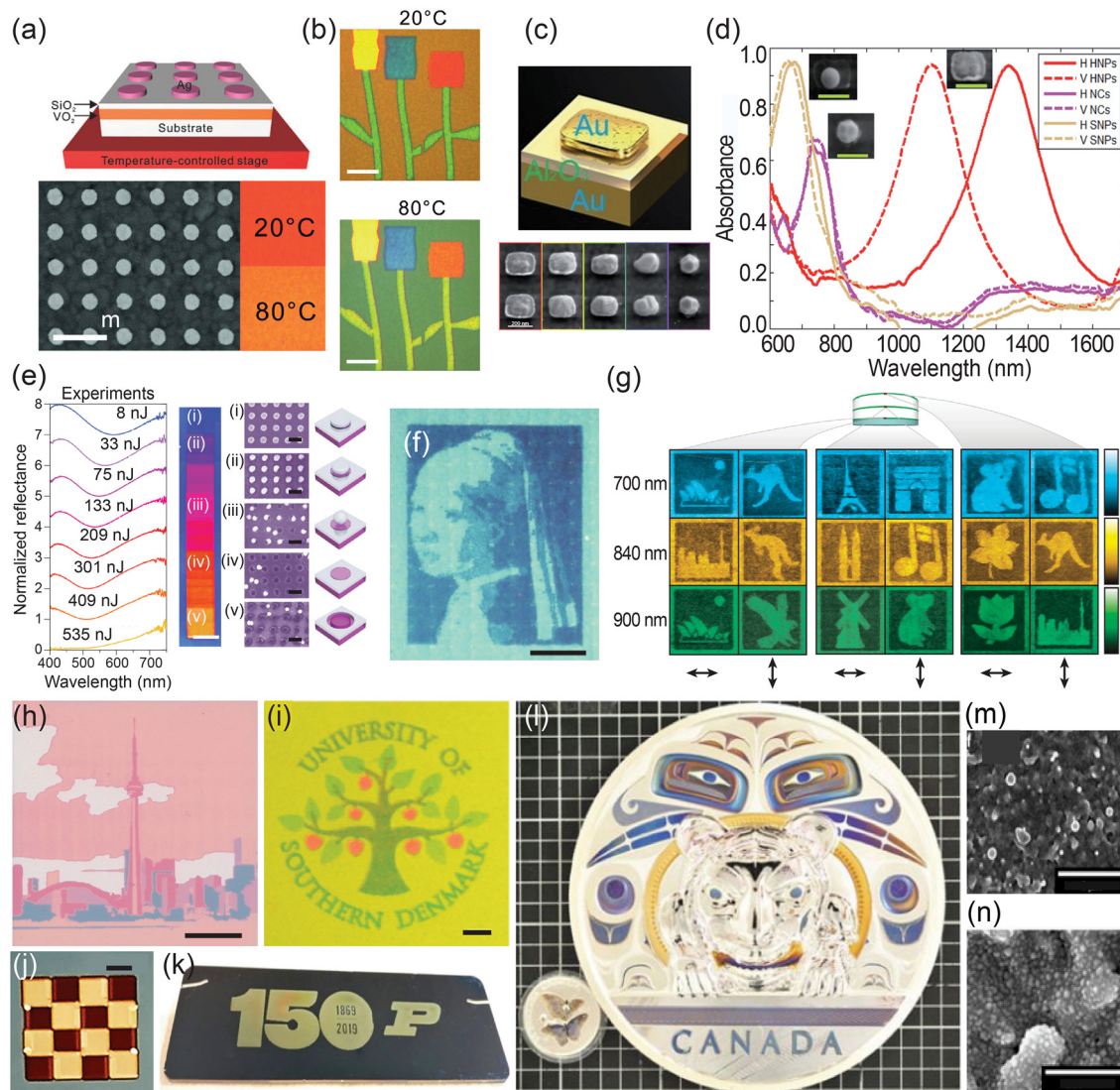


**FIG 8** a) Top: a vanadium dioxide  $\text{VO}_2$ -based device consists of silver  $\text{Ag}$  nanodisk arrays residing on  $\text{SiO}_2$  and  $\text{VO}_2$  layers. Bottom: SEM of the fabricated Ag nanodisk array, and the reflected colors from the metasurface at 20 and 80 °C. b) The reflection images of a pattern made with structure in a) at 20 and 80 °C. a) and b) Reproduced with permission from Shu *et al.*, *Adv. Opt. Mater.* **6**, 7 (2018). Copyright 2018 John Wiley and Sons. c) Top: gap plasmon structure consisting of an Au hexahedron, an  $\text{Al}_2\text{O}_3$  spacer layer, and an Au reflector. Bottom: SEM images of Au hexahedrons after continuous-wave (CW) laser annealing with different intensities. From left to right, laser intensities are 0, 7.3, 9.7, 12.2, and 15.7  $\text{kW cm}^{-2}$ . d) Measured absorbance spectra of the three nanoparticles shown in insets (scale bar: 200 nm). Solid lines represent incident polarization along the horizontal axis along the long axis of the hexahedron in the rightmost inset) and dashed lines along the vertical axis. c) and d) Reproduced with permission from Chen *et al.*, *Nanoscale* **6** (3), 1756 (2014). Copyright 2014 Royal Society of Chemistry. e) Left: measured reflectance spectra of Al nanodisk after pulsed laser irradiation with varying pulse energy. Right: SEM (left column) and 3D diagrams (right column) of Al nanodisks after pulsed laser irradiation with pulse energies of i) 0, ii) 33, iii) 133, iv) 301, and v) 535 nJ. Scale bars: 200 nm. f) An image in blue tone printed by pulsed laser on the metasurface in e), with a resolution of 127 000 dpi. Scale bar: 10  $\mu\text{m}$ . e) and f) Reproduced with permission from Zhu *et al.*, *Nat. Nanotechnol.* **11** (4), 325 (2016). Copyright 2016 Nature Publishing Group. g) A total of 18 patterns are multiplexed into three layers of Au nanorods embedded in polyvinyl alcohol with three wavelengths (700, 840, 980 nm) and two polarizations as indicated. The size of all images is 100 × 100  $\mu\text{m}$ . g) Reproduced with permission from Zijlstra *et al.*, *Nature* **459**, 7245 (2009). Copyright 2009 Nature Publishing Group. h) Demonstration of a large-area laser color printing on a semicontinuous Au film on a glass. A reproduction of a photograph of the skyline of Toronto, Canada, converted into a six-color image file, and each color is mapped to a different scan rate of the laser system. Reproduced with permission from Ooms *et al.*, *Langmuir* **31** (18), 5252 (2015). Copyright 2015 American Chemical Society. i) Bright-field optical microscopy images of a 90 × 90  $\mu\text{m}^2$  color print of the University of Southern Denmark logo viewed with an analyzer copolarized with respect to the polarization of the writing laser beam. Scale bars: 10  $\mu\text{m}$ . Reproduced with permission from Greybush *et al.*, *ACS Nano* **13** (1), 3875 (2019). Copyright 2019 American Chemical Society. j) and k) Demonstration of a large-area femtosecond laser color printing on Ag SMF on Ag mirror with silica spacer. j) Two color checkered pattern and k) 150 years of Purdue logo with a "P" letter. Reproduced with permission from Song *et al.*, *Opt. Mater. Express* **9** (3), 779 (2019). Copyright 2019 Optical Society of America. l) Photograph of a laser-colored 5 kg silver coin of diameter 21 cm and thickness 2.5 cm (a smaller coin with two butterflies is also shown); m) low-magnification and n) high-magnification SEM images of laser modified silver surface. l), m), and n) Reproduced with permission from Guay *et al.*, *Nat. Commun.* **8**, 16095 (2017). Copyright 2017 Nature Publishing Group.

work by Zijlstra *et al.* is based on a similar principle,<sup>107</sup> where randomly dispersed Au nanorods with varying aspect ratio and orientation play the same role as the Al nanodisks and crosses in Zhu's and Zhang's work, respectively. Printing is done by pulsed laser with a select central wavelength and polarization, and nanorods (with matching orientation and aspect ratio) that support surface plasmon resonance (SPR) under such excitation are significantly heated by the laser and reshape. After printing, the pulsed laser creates a trace of reshaped nanorods, whereas those that do not support SPR remain unchanged. Finally, the printed image is readout via raster scanning the same pulsed laser over the printed area and detecting the SPR-mediated two-photon luminescence (TPL) signal. Since the TPL is excited with the same wavelength and polarization as is used for printing, the printed area has a lower TPL signal because of the depletion of nanorods supporting SPR at the readout laser wavelength. Such systems can multiplex images via the print and readout laser wavelength and polarization. In Fig. 8(g), the authors demonstrate 18 different images encoded in three layers of a nanorod/polymer structure with three laser wavelengths and two polarizations. A different approach to laser printing on metasurfaces has been presented by Raza *et al.*<sup>135</sup> The authors fabricate a dual-material metasurface composed of self-assembled polystyrene spheres coated with a continuous silver layer. Next, they postprocess the metasurface using nanosecond laser pulses to define meta-atoms of varying polystyrene-to-silver ratio; thus, they locally change the structure reflectance (optical response from plasmonic to photonic), and realize high-resolution (over 20 000 dpi) color printing. This approach can be used to realize cost effective, large-area structural colors with high resolution.

Another type of plasmonic structures attractive for laser-induced printing is semicontinuous metal films (SMF) comprised of random, fractal-type, island films,<sup>136,137</sup> and SMF deposited on a metallic mirror with a dielectric spacer.<sup>138,139</sup> These films can be fabricated on large substrates using physical vapor deposition (PVD) techniques, and the optical properties of such films can be altered using lasers.<sup>137–140</sup> By combining PVD fabrication techniques and laser-induced postprocessing, large-scale laser printing is realized.<sup>139,140</sup>

Ooms *et al.* studied CO<sub>2</sub>-laser-induced coloration on semicontinuous Au films deposited on glass.<sup>140</sup> They obtained different colors by adjustment of initial film thickness and variation of a scan rate of the laser system. Authors print large scale (6 cm<sup>2</sup>) images [Fig. 8(h)] with *x*-*y* patterning resolutions of ~180 μm and writing speed of 30 mm<sup>2</sup>/min. Recently, continuous<sup>141</sup> and femtosecond<sup>138</sup> laser printing of plasmonic color has been realized with Au SMF deposited on a gold mirror with a dielectric spacer. Berean *et al.* used continuous laser to induce dewetting of Au film above the percolation threshold (the transition from dielectriclike to metal-like) and to control the structure's visible and IR absorption and reflection.<sup>141</sup> Roberts *et al.* took advantage of the fact that ultrathin (~4 nm) electron-beam evaporated Au forms nanosized islands (termed as "near-percolation film") and constructs an Au/SiO<sub>2</sub>/Au gap plasmon structure where the Au islands atop SiO<sub>2</sub> serve the role of optical antennas.<sup>138</sup> As with the previous works on laser modification of e-beam lithography prefabricated plasmonic color substrate, patterns can be generated by scanning a pulsed laser, and the color can be controlled by the laser parameters [Fig. 8(i)]. The laser-induced color changes are polarization sensitive; thus, different color images can be encoded for different linear and circular polarizations. Laser interaction with metallic surfaces can create chiral

nanostructures.<sup>142</sup> Therefore, optical properties of such structures could be strongly dependent on the polarization of light and produce different color images observed when illuminated with, for example, left- and right-hand circular polarization.

Silver SMFs have a potential to produce a broader range of colors than those made of Au, as Ag has no interband absorption in the visible, and the plasmon resonance of a spherical Ag nanoparticle on glass is located in the blue part of the visible spectrum. Recently Nyga *et al.*<sup>139</sup> demonstrated a broad range of colors (from blue through green, yellow, orange, up to red) by utilizing laser-induced color printing on a large scale 10 nm thick Ag SMF on a Ag mirror with a silica spacer. In Fig. 8(j), the authors demonstrate two-color printing on a 1 cm<sup>2</sup> area and one color printing on a 2.5 cm × 7.5 cm substrate. The colors were controlled through varying scan speed, energy density (~10–100 mJ cm<sup>-2</sup> range), and exposure time of a femtosecond laser. Laser printing on SMFs and SMF on a metallic mirror with a dielectric spacer<sup>138–140</sup> significantly reduces the fabrication complexity by eliminating the need for lithography for nanostructures preparation; thus, it can allow inexpensive large area fabrication of color surfaces.

Coloration of metallic surfaces of bulk elements can also be achieved by laser induced random nanostructuring.<sup>143–146</sup> Laser interaction with a metallic surface can lead (through ablation and/or melting) to the formation of various nanofeatures, which can result in vibrant colors observed in reflection. Recently Guay *et al.* reported printing of appealing macroscopic color images on silver and gold coins using picosecond laser pulses [Fig. 8(k)].<sup>145</sup> The laser-induced color of metallic elements depends on the total accumulated fluence, which controls the size and separation distribution of the formed random nanoparticles [Figs. 8(l) and 8(m)]. This technique can be applied to the coloration of surfaces with significant topographic variations and finish. The above technique makes the process attractive for high-throughput printing applications. Similar coloration effect has been recently achieved with a resolution of 450 dpi on silver jewelry pieces using a nanosecond laser.<sup>146</sup>

Temperature-controlled plasmonic color tuning on VO<sub>2</sub> based structure is similar to most other tuning mechanisms—the optical property of a certain component is altered by temperature. However, the color "printing" cases differ from most other tunable plasmonic color displays in that, instead of defining the display patterns during fabrication, the as-prepared color printing plasmonic devices require postfabrication laser printing and reading, granting more freedom for data encryption but less tunability. For the case of laser-induced printing, there exists a trade-off between resolution and writing speed and, thus, the size of the printed image.

#### D. Chemical tuning

Certain chemical reactions cause metal-insulator transitions; thus, they can also be used to tune the plasmonic colors. Among these, the reversible magnesium (Mg, metal)-to-magnesium hydride (MgH<sub>2</sub>, insulator) process has been intensely investigated by the Liu group. In a pioneering work, Duan *et al.* designed a Mg-based plasmonic metasurface, which in the metallic state can reflect vivid colors by controlling the Mg block dimension and spacing.<sup>147</sup> When the metasurface is exposed in an H<sub>2</sub> environment, Mg undergoes a phase transition over time, leading to reflected-color transformation, and all colors eventually turn to white. This is proposed by the authors as a mechanism to display and erase information, which is demonstrated in Fig. 9(a).

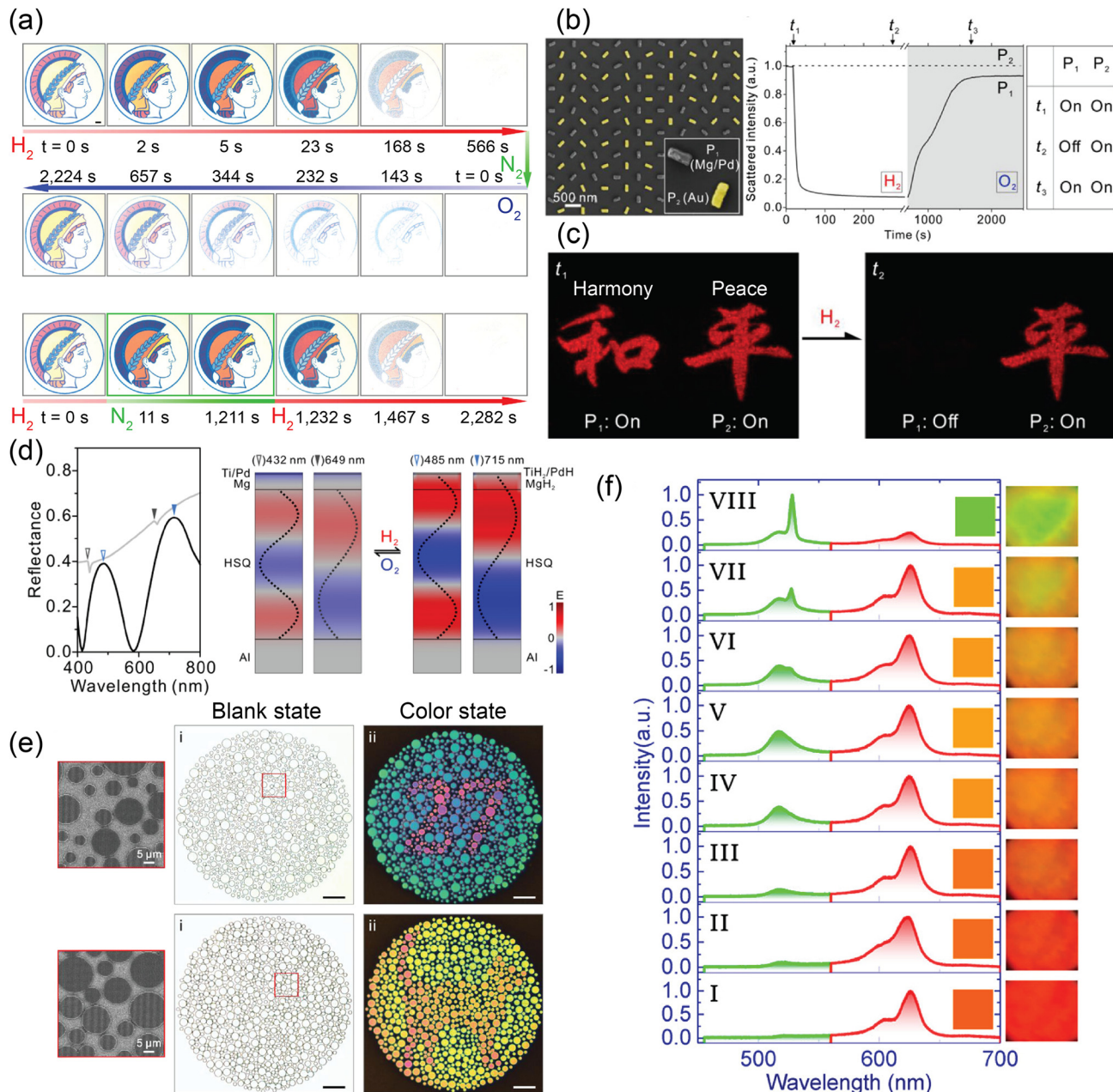


**FIG 9** a) Upper two rows: optical micrographs of the Minerva logo during color erasing with  $H_2$  and restoring with  $O_2$  processes. Bottom row: color “freezing” by switching off hydrogen. a) Reproduced with permission from Duan *et al.*, Nat. Commun. **8**, 14606 (2017). Copyright 2017 Nature Publishing Group. b) Left: SEM showing two phase profiles are constructed with Mg/Pd active pixel,  $P_1$ , gray colored) and Au inactive pixel,  $P_2$ , yellow colored) nanoantennas for two holographic Chinese characters Harmony and Peace. Right: resonant scattered intensities of  $P_1$  and  $P_2$  over time during hydrogenation and dehydrogenation processes.  $P_1$  can be switched on and off while  $P_2$  remains at on state. c) Photographed holographic images for two states where  $P_1$  (harmony) is turned on and off. b) and c) Reproduced with permission from Li *et al.*, Sci. Adv. **4** (6), eaar6768 (2018). Copyright 2018 American Association for the Advancement of Science. d) Simulated reflectance spectra (left plot) and electric field distribution of the different Fabry-Perot resonances (marked in left plot) in the blank (gray curve in spectrum) and color states (black curve in spectrum). e) SEM (left column) and optical microscopic images of the Ishihara display in the blank (middle column) and color (right column) states of “27” (upper row) and a cat (lower row). Scale bars in optical microscopic images: 50  $\mu$ m. d) and e) Reproduced with permission from Chen *et al.*, Nano Lett. **17** (9), 5555 (2017). Copyright 2017 American Chemical Society. f) Measured reflectances spectra (left column) and photographed colors (right column) of the MAPbBr<sub>3</sub> gratings at different pumping intensities, with photoluminescence spectrum marked in green and gratings-reflected background spectrum marked in red. Insets: calculated colors according to the measured spectra. f) Reproduced with permission from Gao *et al.*, ACS Nano **12** (9), 8847 (2018). Copyright 2018 American Chemical Society. The paper is located at <https://pubs.acs.org/doi/abs/10.1021/acsnano.8b02425>. For further information regarding reuse permissions please contact ACS.

A multicolor image is first erased by loading H<sub>2</sub>, and the image is restored with high fidelity by loading O<sub>2</sub>. In the same work, the authors demonstrate information encryption with a metasurface consisting of two types of antennas, active and inactive to H<sub>2</sub>, so that different information states can be revealed before and after hydrogenation. The same principle is applied in a separate effort to construct a multiplexed holography metasurface, with two independent phase profiles encoded by H<sub>2</sub>-active Mg/Palladium (Pd) antennas and H<sub>2</sub>-inactive Au antennas.<sup>148</sup> As such, information encoded by the active antennas can be manually turned on or off by H<sub>2</sub> and O<sub>2</sub>, while that by the inactive antennas remains unperturbed [Figs. 9(b) and 9(c)]. By cleverly designing a dash-dot system with active and inactive antennas, the authors demonstrate a method to encode all ten numerical digits in a metasurface, which can be decrypted by a specialized “key”—a combination of H<sub>2</sub>/O<sub>2</sub> gas and left/right circularly polarized (LCP/RCP) light.

Aside from plasmonic antennas, a titanium (Ti)/Pd/Mg hybrid layer is also used by the same research group to control the reflected colors from Fabry–Perot (FP) cavities. Chen *et al.* demonstrated a metasurface with HSQ pillars of varying heights capped by a Ti/Pd/Mg hybrid layer.<sup>149</sup> In this metasurface, when the capping layer is metallic, all pillars are broadband reflectors, and white color is reflected. In contrast, when the metasurface is loaded with H<sub>2</sub>, the capping layer becomes dielectric. This causes each pillar to form an FP cavity, and the reflected color is well controlled by the height of the HSQ pillar [i.e., length of the cavity, Fig. 9(d)]. Owing to the sharp FP resonances, the generated colors are more brilliant and cover a wider gamut than those from Mg plasmonic metasurface. As can be observed from Fig. 9(e), the metasurface can turn from a completely featureless blank-state to a color-state with rich colors and high contrast. One key difference from Ref. 147, however, is that in this work H<sub>2</sub> is used to uncover information while in Ref. 147 it is used to erase information.

Although the Mg- and MgH<sub>2</sub>-based metasurfaces are capable of generating colors with high purity and a wide gamut, the chemistry-tuning process is in general a slow process. For example, it takes 566 s of hydrogenation to erase the image in Fig. 9(b) and 2224 s to fully restore it. Instead of inducing optical changes chemically, Gao *et al.* recently proposed a “photon doping” mechanism to tune the reflected color of a perovskite-based metasurface in nanosecond time scale.<sup>150</sup> The proposed device requires two light sources for color tuning—a background white light and a pulsed pumping laser. The perovskite material (methylammonium lead halide perovskite, MAPbBr<sub>3</sub>, where MA = CH<sub>3</sub>NH<sub>3</sub><sup>+</sup>) is patterned into one-dimensional gratings to reflect a certain color of the background white-light source. Meanwhile, the intrinsic photoluminescence (PL) in MAPbBr<sub>3</sub> is triggered by the pump laser. Although the reflected background color is not dynamically tunable (determined by the gratings structure), the PL spectrum and strength are controlled by the pump laser intensity [Fig. 9(f)]. According to the color mixing theory, a third color can be generated by mixing two colors, and the hue is governed by the mixing ratio. Consequently, various colors can be generated with a broadband white light source and a pumping laser of different intensities, with the transition time determined only by the buildup and ringdown time of the PL which are in the nanosecond scale.

### E. Mechanical tuning

Another method to produce strongly tunable plasmonic colors is via reversible deformation of metasurfaces. The simplest approach is

to place metasurfaces on stretchable substrates. By stretching the substrate, the metasurface layout is modified, thereby changing its optical response. There are three major classes of such stretchable devices: nanoparticle-based,<sup>151–154</sup> grating-based,<sup>155–157</sup> and nanostructured surfaces.<sup>158–161</sup> As flexible substrate fabrication methods are developed, alternative kinds of plasmonic devices are being investigated to realize reversible color tuning.<sup>162–167</sup>

Metallic nanoparticles support strong LSPR when isolated, and near field plasmonic coupling occurs if they are brought close together. This coupling shifts the resonance away from the LSPR wavelength of the isolated nanoparticles. Additionally, the coupled modes are sensitive to the interparticle spacing. By stretching the substrate, the interparticle spacing is changed, which leads to large spectral shifts in the optical response of the nanoparticle-loaded surface. Generally, these devices are fabricated via functionalization of a polydimethylsiloxane (PDMS) substrate, followed by immersion into a colloidal nanoparticle solution. This facilitates the attachment of the nanoparticles to the substrate without overlapping.<sup>168</sup> Alternatively, dense monolayers of nanoparticles may be formed at the interface between certain liquids and bond to PDMS.<sup>152,153</sup> Additional tuning of the nanoparticle size and spacing may be achieved by further growing the bonded nanoparticles. The simple fabrication methods of these devices make them attractive for prototyping or mass production. This class of surfaces typically operates at a wavelength of ~550 nm with a tuning range of around 60 nm, and the FWHM of these systems is approximately that of the isolated nanoparticle resonance (~150 nm). However, the light interaction efficiency of these surfaces is generally well below 20%. An example of such a structure and its spectral response upon stretching are shown in Fig. 10(a). The major advantage of this approach is the ease of fabrication since it does not require any expensive pattern transfer or electron-beam lithography (EBL) techniques.

As discussed in Sec. III A, metallic gratings present another example of plasmonic system that exhibits a color shift with the change in periodicity.<sup>155–157</sup> To achieve tunability, gratings are fabricated on the stretchable substrates; thus, the periodicity of the grating—thereby the plasmonic resonant wavelength—changes when the substrate is stretched. There are a variety of methods to fabricate such gratings on flexible substrates, the simplest of which is described in the work of Olcum *et al.*<sup>157</sup> In this work, a master grating is created on Si, and a PDMS grating is fabricated by casting onto the master. Subsequently, the PDMS grating is coated in Ag to form plasmonic and stretchable Ag gratings. More complex methods of fabrication involve prestraining a PDMS substrate and treating it with argon (Ar) plasma which causes the substrate to develop sinusoidal patterns to relieve stress when released. This rippled surface is then coated with Ag. When stress is reapplied, it causes cracks, and the cracked Ag-coated surface forms a nanowire array grating.<sup>155</sup> These systems operate by only allowing for SPP excitation when the proper momentum matching conditions are met, which are dependent on the periodicity of the gratings. By stretching the substrate and thus enlarging the grating periodicity, the SPP coupling wavelength shifts. Since most of the surface is covered by a plasmonic metal layer at some strain level, the film will crack or delaminate. For example, at 23% strain the Ag will elastically deform or crack. This is the ultimate limit for the tuning range of such grating structures in practical situations. The advantage of using a grating structure as compared to other approaches is the relatively simple fabrication with excellent tuning performance.

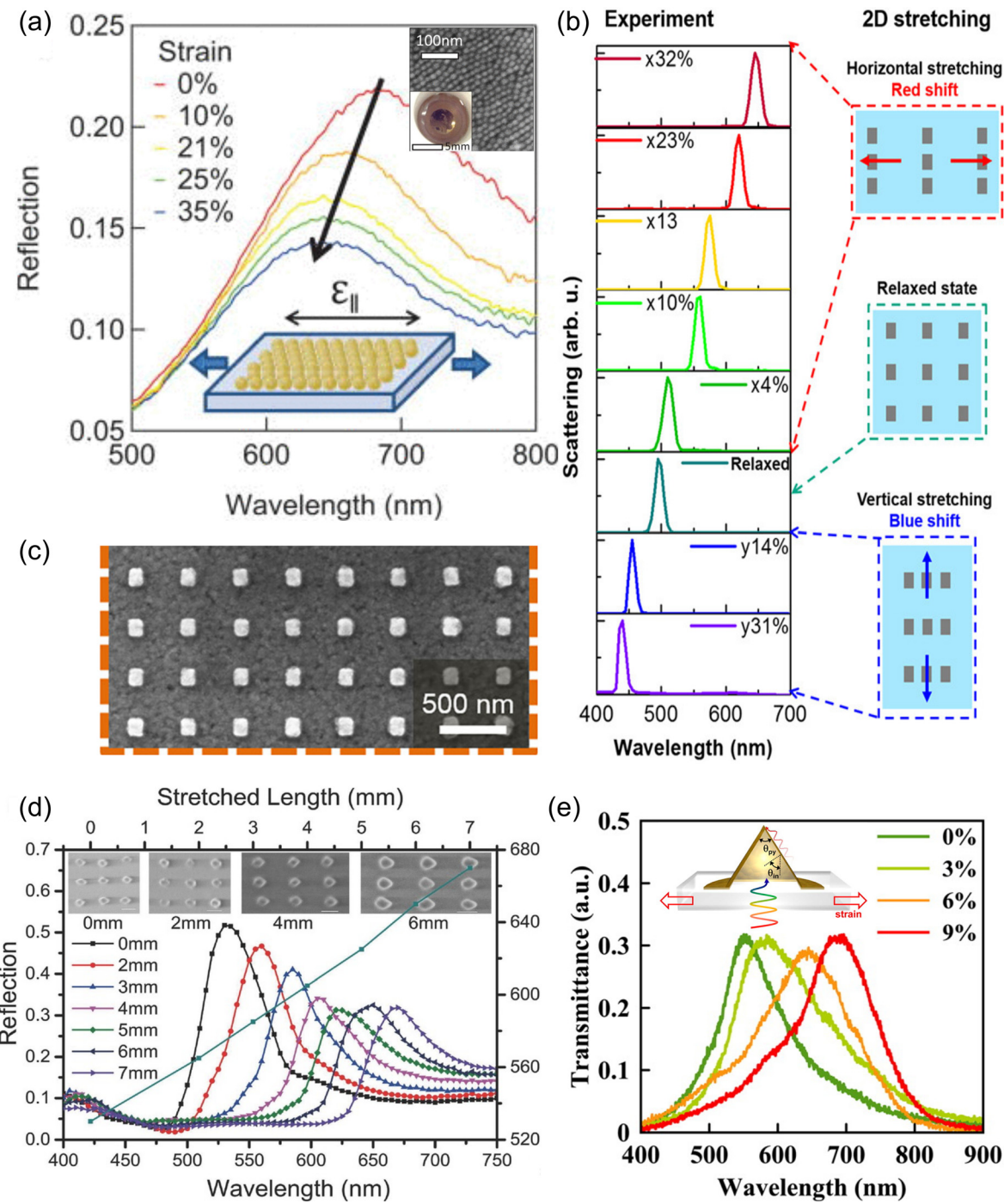


**FIG 10** a) Spectral response of the nanoparticle based device shown in the SEM inset upon stretching, and the cartoon inset shows the schematic of the device being stretched. a) Reproduced with permission from Tseng *et al.*, *Nano Lett.* **17** (10), 6034 (2017). Copyright 2017 American Chemical Society. b) Spectral response of the nanostructures, pictured in c), upon stretching is shown on the left side, on the right the stretching direction is pictured. c) SEM of Al nanostructures on Si before template stripping. These nanostructures are then transferred to PDMS. b) and c) Reproduced from Millyard *et al.*, *Appl. Phys. Lett.* **100** (7), 073101 (2012), with the permission of AIP publishing. d) Spectral response of nanodisks on PDMS (shown in inset SEM images) at different stretch lengths; the green line shows the peak position shift (units on right in nanometers). d) Reproduced with permission from Song *et al.*, *Adv. Opt. Mater.* **5** (9), 1600829 (2017). Copyright 2017 John Wiley and Sons. e) Spectral response of template stripped pyramid structures (shown in inset). e) Reproduced with permission from King *et al.*, *ACS Nano* **9** (11), 10628 (2015). Copyright 2015 American Chemical Society. This paper may be viewed at <https://pubs.acs.org/doi/full/10.1021/acsnano.5b05279> and inquiries regarding permissions should be addressed to ACS.

Additionally, different color ranges may be achieved simply by changing the initial periodicity of the gratings.

The previously mentioned stretchable devices have all been fabricated through self-assembly or casting. There is another class of stretchable color device in which the plasmonic elements are comprised of patterned nanostructures.<sup>158–161</sup> Such devices typically exhibit much more versatility in their behavior and performance. This property is due to the increased control of both the dimensions of the plasmonic nanoantennas and their placement during fabrication. The dimensional control allows for the tuning of the individual antenna resonances, while the engineering of the array geometry allows for the tuning of spatially dispersed modes. An excellent example of what can be achieved in terms of plasmon resonance control is the work of Song *et al.* as shown in Fig. 10(c).<sup>159</sup> This device consists of Al nanodisks patterned by interference photolithography and transferred onto PDMS by a standard template stripping method. The Al nanodisks have a radius of 151 nm and a periodicity of 322 nm, which is well below the wavelength of the incoming light. At zero strain, the disks are strongly coupled due to their tight spacing. This coupling causes a redshift in the resonant wavelength relative to an isolated disk. As the substrate is strained, the coupling between disks decreases, leading to a blue shift in the output resonance. Another feature of lattice resonances is the significantly lower FWHM compared to randomly dispersed nanoparticle arrays (FWHM ~150 nm). This device also exhibits a relatively high reflectance of ~35–50% at the resonant wavelength, which is on the order of that to be expected from gratings and significantly higher than nanoparticle-based surfaces.

Another recent work by Tseng *et al.*<sup>158</sup> uses an Al rectangles template stripped onto a PDMS substrate. This work demonstrated a method to broaden the color palette by making use of the different optical responses at different stretch directions. This device features one of the widest tuning ranges of any PDMS stretchable system thus far, with a coverage of 76% of the human vision color space from red to blue (440–645 nm). This device functions by utilizing rectangular Al scatterers which exhibit broad reflectivity across the optical spectrum. The reflection spectrum is then narrowed by diffraction in the far field. By limiting the collection angle, the FWHM of the spectrum reaches ~20 nm [Fig. 10(b)], which is smaller than the majority of the other devices reviewed (100+ nm). The two-dimensional tuning works in the following way: when the PDMS is stretched parallel with the incident light polarization, the reflected color red shifts with the increasing periodicity. However, when the PDMS is stretched perpendicular to the incident light polarization, the PDMS compresses parallel to the incoming polarization, blue shifting the resonance by decreasing the periodicity. However, this performance comes at the cost of very narrow angle of operation as would be expected from diffraction-based tunable surfaces of this type. Additionally, the scattering efficiency, which is defined as the amount of light scattered at a particular wavelength divided by the amount collected, is only 5% due to the narrow collection angle.

Aside from flat nanostructures, methods to create 3D nanostructures have also been explored.<sup>162–167</sup> In 2015, the Yoo research group designed and fabricated 3D Si molded Au pyramids on PDMS [Fig. 10(e)]. These pyramids exhibit a large ~150 nm tuning range from 545 to 682 nm upon stretching only 9%. This structure is more sensitive to strain than any other structure in this review. The sensitivity derives from the plasmonic Kretschmann-like coupling geometry

formed by the Au pyramids. This coupling geometry is extremely sensitive to the incident angle of light. As the substrate is stretched, the angle of the pyramid walls changes, shifting the resonant position. This method of fabricating structures is compatible with roll-to-roll processing and holds potential for large scale manufacturing, making it an interesting avenue in the realm of plasmonic tunable color devices.

Overall, plasmonic structures placed on flexible substrates have proven to be a fascinating way to directly study the effects of period on plasmonic resonance. Additionally, many of the structures outlined in this section are quite amenable to large scale manufacturing and are generally low-cost relative to their tuning performance. However, there are several limitations inherent in flexible systems. All of the systems in this review do not have back reflectors. This is in part due to the fact that a solid reflective surface would not survive the deformations needed to get the tuning desired. As a result, these flexible systems tend to have optical efficiencies that are quite low. Additionally, there is a significant loss of signal intensity with stretching [see Figs. 10(b)–10(e)]. This is because the density of the optical components decreases linearly with strain, leading to less interaction with incoming light [Fig. 10(b) has normalized peaks]. Another limitation of this approach is that while the system is tunable, this tuning is generally done by clamping the film to a linear actuator which stretches the system. Therefore, the entire tuning system is rather bulky and complicated. This, of course, can be overcome by exploring ways to integrate actuators with the developed flexible system. Finally, these works do not explore the effects of repeated stretching on both the adhesion of the nanostructures and the mechanical stability of the film. In short, this method of tuning has proven remarkable in its color tuning ability but several important areas remain for further research such as many-cycle stability, integrated tuning methods, and how to boost the optical efficiency while preserving the tuning range. These must be addressed before such research can enter the realm of useful application.

## F. MEMS and NEMS tunable plasmonic devices

There has been some effort to introduce microelectromechanical (MEMS) and nanoelectromechanical (NEMS) systems as active color filtering mechanisms.<sup>169,171–178</sup> This is challenging considering that the size of a plasmonic antenna is less than half of the wavelength of visible light. Therefore, the antenna size is generally 300 nm or less if the device operating wavelength is around 600 nm. The gap sizes are also small to allow for near field coupling. Such small sizes of these structures mean that the fabrication tolerances must be very small for MEMS and NEMS devices. The vast majority of these kinds of tunable devices operate in the terahertz regime where the size scales of the plasmonic resonators and gaps are more amenable to fabrication.<sup>171,179</sup> Some of the only MEMS devices, with tuning in the visible range, were fabricated by the Sawada group.<sup>169,172,173</sup> One of the devices developed and its optical performance is shown in Figs. 11(a)–11(c).<sup>169</sup> Based on MEMS electrostatic comb drive actuators, this device can shift the transmission peak from 542 to 668 nm with an FWHM of ~100 nm and a modulation depth of about 20%. The voltage required is ~60 V at maximum. Their device illustrates one of the big challenges facing MEMS-based devices: the poor scaling of many forces at the nanoscale. Therefore, the size of the actuator

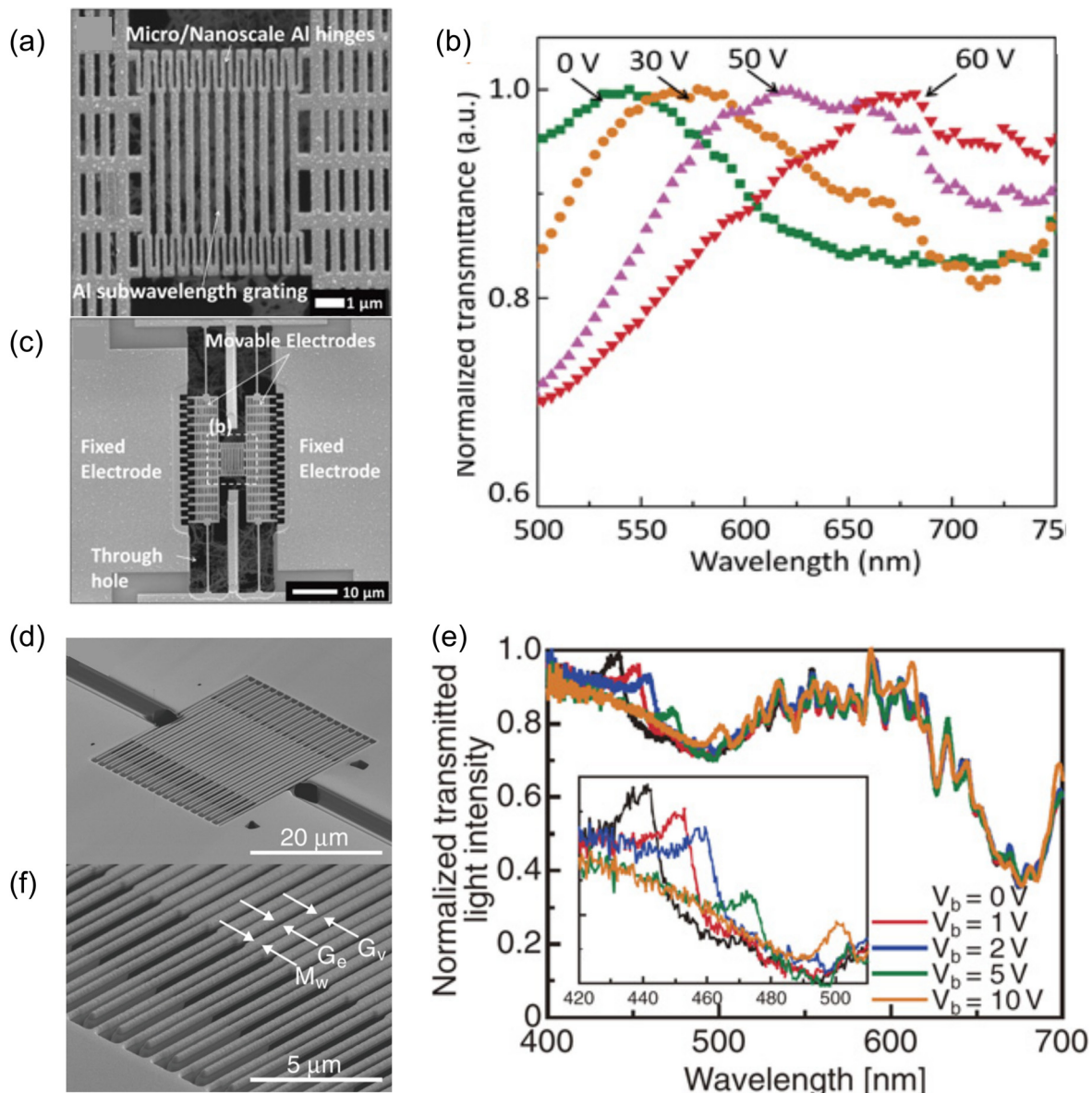


**FIG 11** a) Zoomed-in view of subwavelength plasmonic grating. b) Spectral response of device shown in a) and c) under different drive voltages. c) Zoomed-out view of electrostatically tunable nanograting. a)–c) Reproduced with permission from Honma *et al.*, Appl. Phys. Express **9**, 027201 (2016). Copyright 2016 Institute of Physics Science. d) Zoomed-out view of electrostatic grating device with grating and electrostatic drive integrated. e) Spectral response under different drive voltages; tuning occurs between 400 and 500 nm shown in inset). f) Zoomed-in view of the integrated electrostatic grating. d)–f) Reproduced with permission from Yamaguchi *et al.*, Appl. Phys. Express **7** (1), 012201 (2014). Copyright 2014 Institute of Physics Science.

required to drive this device is  $\sim 10$  times larger than the actual optical device. As a result, the optical efficiency of such devices under flood illumination is limited simply due to surface area concerns. An alternate method is to utilize gratings in which the alternating fingers of the grating are oppositely charged causing deformation of the grating.<sup>170</sup> This device and its optical performance are shown in Figs. 11(d)–11(f). This method has the advantage of not requiring a separated actuator like the comb drive

based actuators. It has a tuning range of  $\sim 60$  nm and is able to operate at around 480 nm. However, the modulation contrast is only  $\sim 10$ , and from 550 to 650 nm the intensity of transmitted light is equivalent to the transmitted light intensity at resonance. Therefore, this device has very poor color purity. This is a relatively new and extremely challenging multidisciplinary area which promises to have a large impact given the flexibility of MEMS devices and tuning compared to alternative approaches.

## V. OUTLOOK AND CONCLUSIONS

### A. Applications and outlook

Static color metasurfaces based on subwavelength gratings and nanopatches, nanodisk arrays, nanodisk and hole arrays, and GSP based structures have a number of excellent properties such as high spatial resolution, viewing angle independence, environmental friendliness, and scalable manufacturability. Aside from these static surfaces as outlined in Sec. III, tunable plasmonics based on electrical, thermal, laser, chemical, MEMS/NEMS, and mechanical stretch tuning have all been developed over that past few years. These devices share many of the same advantages as their static predecessors while also being tunable.

The advantageous properties of plasmonic devices lead to a number of possible practical functionalities. For example, as compatibility with metal-oxide-semiconductor (CMOS) camera sensor pixels in electronic devices are scaled down, the traditional method of color filtering via dye is becoming untenable. This problem occurs due to the increasingly difficult multiple-aligned lithography steps required. Additionally, dye's low absorption coefficient requires relatively thick, difficult-to-fabricate structures with high aspect ratios, causing a broad range of associated manufacturing and design problems. Plasmonic structures, on the other hand, are ultrathin, and their spatial resolution goes beyond the diffraction limit, completely bypassing the issues with scaling down the absorptive dye filters. Finally, many of these dyes could be toxic to the environment when the device lifetime is over and should be discarded, whereas the plasmonics elements are made of recyclable or biodegradable materials.<sup>87,180,181</sup>

Other applications exploiting both the tunability of plasmonics and their extremely high spatial resolution are in devices that require extremely dense patterning that includes, for example, high-resolution image recording and laser printing via the controlled modification of plasmonic surfaces with lasers.<sup>133–135,138–140,143–146</sup> Additionally, by exploiting polarization tuning, plasmonic metasurfaces gain an additional degree of freedom allowing for data storage capacity to be increased in color-based information storage systems.<sup>107,108</sup> Also, polarization-tunable devices can be used in the birefringent screening of skin cancer tissue.<sup>101,109</sup> Finally, polarization tuning enables three-dimensional (3D) stereoscopic color printing<sup>105</sup> and encryption of messages that can be only decrypted by having the correct “polarization keys.”<sup>104</sup> Perhaps the most visually striking usage of tunable high-resolution plasmonics is in the development of high-end color displays. These displays have the potential to consume less power while operating within a broader color space as compared to other technologies such as e-ink.<sup>29</sup>

Aside from these applications, there is a huge potential for biological, chemical, and mechanical research as many of the mechanisms outlined for tuning plasmonic colors could be utilized for sensing. For example, flexible substrate strain tuning of color is inherently also a strain sensor. Such sensors, which operate in the visible, can be used for naked eye measurement of stress and strain. Additionally, such sensors can be much smaller than conventional resistive strain gauges allowing for in-depth characterization of materials at minute scales.<sup>156,182</sup> Another area where plasmonic visible light sensing makes a significant impact is biology. Nanostructured plasmonic elements and particles are sensitive enough to their near-field environment to be capable of measuring the refractive index shift from biological macromolecules and various other chemical species.<sup>183–187</sup> By using dense

arrays of plasmonic nanostructures, images of chemical movements within single cells have been measured.<sup>188</sup> Hence, the future for extremely small and highly sensitive sensors built on visual plasmonics is extremely bright.

As an outlook, the inherent optical loss in metals and the radiation loss of plasmonic structures inevitably broaden the resonant linewidth, thereby decreasing the efficiency and reducing color saturation. One possible solution is to use Al to construct color metasurfaces instead of the more commonly used plasmonic materials Au and Ag. The abundance of Al and its compatibility with metal-oxide-semiconductor (CMOS) processes have accelerated the development of the Al-based plasmonic color filters in research and promise a bright future for their commercialization. Another solution for the improvement of color vibrancy is the introduction of Fano resonances or plasmon hybridization.<sup>39</sup> The high quality factor (Q-factor) resonance (narrow resonant linewidth) not only increases color saturation but also offers an opportunity to generate colors beyond the sRGB region on the CIE diagram by varying the periodicity of the structure, broadly increasing the color gamut. As shown in a recent work,<sup>39</sup> high-efficiency narrowband resonance (FWHM of ~16 nm) enabled by SPP-LSP hybridization results in vibrant colors which can be continuously modified by varying the ambient environment. As researchers make progress into these directions, ever brighter and more sensitive sensors, displays, data storage, and encryption systems will be enabled and commercialized.

### B. Conclusions

In conclusion, metallic nanostructures show great potential for creating colorful plasmonic elements. By virtue of efficient simulation methods and advanced nanofabrication technologies, the geometry of the metallic nanoantennas can be determined with optimized parameters and precisely controlled by advanced fabrication methods. As exemplified by some popular constructions such as gratings, nanohole arrays, MIM sandwiched resonators, and hole-disk pairs, plasmonic color filters present a range of advantageous features compared with the conventional pigments and nonplasmonic structural colors, which include subdiffraction spatial resolution, nontoxic material components, ultracompact architectures, and long-term durability. In addition to these passive devices, a wide variety of dynamically tunable plasmonic colors was reviewed. In particular, we reviewed tunable plasmonics based on polarization, electricity, heat, chemical reaction, mechanical stretching, and MEMS/NEMS, discussing the advantages and limitations of each tuning mechanism. Tunable plasmonics leverage many of the same benefits as passive colors but expand the functionality and applications space of plasmonic colors significantly. Applications such as switchable or encrypted color tags, high-density data storage, information multiplexing, plasmonic animations, and ultralow power full-color passive displays are now being intensely researched due to recent developments in tunable plasmonics.

However, all of the devices outlined need significant research to expand their color palette, light handling efficiency performance, power consumption, viewing angle, and other factors before they will become commercially viable. As a result, vigorous research is being conducted on methods to improve on these weaknesses, such as the exploitation of different plasmonic modes which exhibit higher performance such as Fano modes and hybrid plasmonic modes.

Additionally, development and usage of materials which exhibit better performance such as Al will also improve performance and cost.

This is an exciting time to research into plasmonic coloring as the technological capability of this field and the demand for high-performance optical systems have neatly overlapped. Furthermore, due to the increasing demands for innovative photonic technologies such as switchable displays, optical cryptography, camouflage, chemical and biological sensors, and high-density data storage systems, investigations of dynamically tunable plasmonic color filters are being pursued extensively. The authors expect that soon plasmonic color technology will span a full spectrum of applications in our daily lives.

## ACKNOWLEDGMENTS

M.S. would like to acknowledge the Chinese Scholarship Council (CSC, No. 201606050044) for financial support. M.S. and H.Y. acknowledge the support by the National Natural Science Foundation of China (No. 61575032). S.P. would like to acknowledge support by the Department of Defense (DoD) through the National Defense Science & Engineering Graduate Fellowship (NDSEG) Program. P.N. would like to acknowledge support by the Polish-U.S. Fulbright Commission through the Fulbright Senior Award Scholarship in the 2018–2019 academic year. Purdue co-authors would like to acknowledge support from the Air Force Office of Scientific Research MURI Grants (Nos. FA9550-14-1-0389 and FA9550-17-1-0243) and DARPA/DSO Extreme Optics and Imaging (EXTREME) program (No. HR00111720032).

## REFERENCES

- <sup>1</sup>S. Furukawa, T. Masui, and N. Imanaka, “Synthesis of new environment-friendly yellow pigments,” *J. Alloys Compd.* **418**(1–2), 255–258 (2006).
- <sup>2</sup>A. V. Whitney, R. P. Van Duyne, and F. Casadio, “An innovative surface-enhanced Raman spectroscopy (SERS) method for the identification of six historical red lakes and dyestuffs,” *J. Raman Spectrosc.* **37**(10), 993–1002 (2006).
- <sup>3</sup>Y. Huo, C. C. Fesenmaier, and P. B. Catrysse, “Microlens performance limits in sub-2-μm pixel CMOS image sensors,” *Opt. Express* **18**(6), 5861 (2010).
- <sup>4</sup>M. C. Gather, A. Köhnen, A. Falcon, H. Becker, and K. Meerholz, “Solution-processed full-color polymer organic light-emitting diode displays fabricated by direct photolithography,” *Adv. Funct. Mater.* **17**(2), 191–200 (2007).
- <sup>5</sup>H.-S. Koo, M. Chen, and P.-C. Pan, “LCD-based color filter films fabricated by a pigment-based colorant photo resist inks and printing technology,” *Thin Solid Films* **515**(3), 896–901 (2006).
- <sup>6</sup>M. Burresi *et al.*, “Bright-white beetle scales optimise multiple scattering of light,” *Sci. Rep.* **4**(1), 6075 (2015).
- <sup>7</sup>P. Vukusic and J. R. Sambles, “Erratum: Photonic structures in biology,” *Nat.* **424**(6950), 852–855 (2003).
- <sup>8</sup>S. Kinoshita and S. Yoshioka, “Structural colors in nature: The role of regularity and irregularity in the structure,” *ChemPhysChem* **6**(8), 1442–1459 (2005).
- <sup>9</sup>R. O. Prum, R. L. Morrison, and G. R. Ten Eyck, “Structural color production by constructive reflection from ordered collagen arrays in a bird (*Philepitta castanea*: Eurylaimidae),” *J. Morphol.* **222**(1), 61–72 (1994).
- <sup>10</sup>Y. Zhao, Z. Xie, H. Gu, C. Zhu, and Z. Gu, “Bio-inspired variable structural color materials,” *Chem. Soc. Rev.* **41**(8), 3297–3317 (2012).
- <sup>11</sup>Y. Ding, S. Xu, and Z. L. Wang, “Structural colors from Morpho peleides butterfly wing scales,” *J. Appl. Phys.* **1**(6(7)), 074702 (2009).
- <sup>12</sup>H. Ghiradella, “Light and color on the wing: Structural colors in butterflies and moths,” *Appl. Opt.* **3** (24), 3492 (1991).
- <sup>13</sup>P. Vukusic, R. Sambles, C. Lawrence, and G. Wakely, “Sculpted-multilayer optical effects in two species of *Papilio* butterfly,” *Appl. Opt.* **4** (7), 1116 (2001).
- <sup>14</sup>S. Kinoshita, S. Yoshioka, and J. Miyazaki, “Physics of structural colors,” *Rep. Prog. Phys.* **71**(7), 076401 (2008).
- <sup>15</sup>P. Sciau, “Nanoparticles in ancient materials: The metallic lustre decorations of medieval ceramics,” in *The Delivery of Nanoparticles* (InTech, Rijeka, 2012), Chap. 25.
- <sup>16</sup>I. Freestone, N. Meeks, M. Sax, and C. Higgitt, “The Lycurgus cup—A roman nanotechnology,” *Gold Bull.* **4** (4), 270–277 (2007).
- <sup>17</sup>S. Perez-Villar, J. Rubio, and J. L. Otero, “Study of color and structural changes in silver painted medieval glasses,” *J. Non-Cryst. Solids* **354**(17), 1833–1844 (2008).
- <sup>18</sup>I. Angelini *et al.*, “Chemical analyses of Bronze Age glasses from Frattesina di Rovigo, Northern Italy,” *J. Archaeol. Sci.* **31**(8), 1175–1184 (2004).
- <sup>19</sup>G. Artioli, I. Angelini, and A. Polla, “Crystals and phase transitions in protohistoric glass materials,” *Phase Transitions* **81**(2–3), 233–252 (2008).
- <sup>20</sup>N. Brun, L. Mazerolles, and M. Pernot, “Microstructure of opaque red glass containing copper,” *J. Mater. Sci. Lett.* **1** (23), 1418–1420 (1991).
- <sup>21</sup>J. Perez-Arantegui *et al.*, “Luster pottery from the thirteenth century to the sixteenth century: A nanostructured thin metallic film,” *J. Am. Ceram. Soc.* **84**(2), 442–446 (2004).
- <sup>22</sup>T. W. Ebbesen, H. J. Lezec, H. F. Ghaemi, T. Thio, and P. A. Wolff, “Extraordinary optical transmission through sub-wavelength hole arrays,” *Nature* **391**(6668), 667–669 (1998).
- <sup>23</sup>M. Song *et al.*, “Conversion of broadband energy to narrowband emission through double-sided metamaterials,” *Opt. Express* **21**(26), 32207 (2013).
- <sup>24</sup>M. Song *et al.*, “Nanofocusing beyond the near-field diffraction limit via plasmonic Fano resonance,” *Nanoscale* **8**(3), 1635–1641 (2016).
- <sup>25</sup>E. Hutter and J. H. Fendler, “Exploitation of localized surface plasmon resonance,” *Adv. Mater.* **16**(19), 1685–1706 (2004).
- <sup>26</sup>K. Kumar, H. Duan, R. S. Hegde, S. C. W. Koh, J. N. Wei, and J. K. W. Yang, “Printing colour at the optical diffraction limit,” *Nat. Nanotechnol.* **7**(9), 557–561 (2012).
- <sup>27</sup>M. K. Hedayati and M. Elbahri, “Review of metasurface plasmonic structural color,” *Plasmonics* **12**(5), 1463–1479 (2017).
- <sup>28</sup>A. Kristensen *et al.*, “Plasmonic colour generation,” *Nat. Rev. Mater.* **2**(1), 16088 (2017).
- <sup>29</sup>L. Shao, X. Zhuo, and J. Wang, “Advanced plasmonic materials for dynamic color display,” *Adv. Mater.* **3** (16), 1704338 (2018).
- <sup>30</sup>T. Xu, H. Shi, Y.-K. Wu, A. F. Kaplan, J. G. Ok, and L. J. Guo, “Structural colors: From plasmonic to carbon nanostructures,” *Small* **7**(22), 3128–3136 (2011).
- <sup>31</sup>Y. Gu, L. Zhang, J. K. W. Yang, S. P. Yeo, and C.-W. Qiu, “Color generation via subwavelength plasmonic nanostructures,” *Nanoscale* **7**(15), 6409–6419 (2015).
- <sup>32</sup>G. Wyszecki and W. S. Stiles, *Color Science: Concepts and Methods, Quantitative Data and Formulae*, 2nd ed. (Wiley, New York, NY, 1982).
- <sup>33</sup>C. Abraham, <https://medium.com/hipster-color-science/a-beginners-guide-to-colorimetry-401f1830b65a> for “A Beginner’s guide to (CIE) Colorimetry,” 2017.
- <sup>34</sup>C. A. Poynton, *Digital Video and HDTV Algorithms and Interfaces* (Elsevier, San Francisco, 2003).
- <sup>35</sup>RP 431-2:2011—SMPTE Recommended Practice—D-Cinema Quality—Reference Projector and Environment (The Society of Motion Picture and Television Engineers, New York, 2011).
- <sup>36</sup>M. Wuerthele, <https://appleinsider.com/articles/16/09/09/apples-wide-color-screen-on-the-iphone-7-will-lead-to-more-faithful-color-reproduction> for “Apple’s Wide Color screen on the iPhone 7 will lead to more faithful color reproduction,” 2016.
- <sup>37</sup>R. M. Soneira, [http://www.displaymate.com/Galaxy\\_Note7\\_ShootOut\\_1.htm](http://www.displaymate.com/Galaxy_Note7_ShootOut_1.htm) for “Galaxy Note7 OLED Display Technology Shoot-Out.”
- <sup>38</sup>W. Sabra, S. I. Azzam, M. Song, M. Povolotskyi, A. H. Aly, and A. V. Kildishev, “Plasmonic metasurfaces for subtractive color filtering: Optimized nonlinear regression models,” *Opt. Lett.* **43**(19), 4815 (2018).
- <sup>39</sup>M. Song *et al.*, “Color display and encryption with a plasmonic polarizing metamirror,” *Nanophotonics* **7**(1), 323–331 (2018).
- <sup>40</sup>C. Huang *et al.*, “Reconfigurable metasurface cloak for dynamical electromagnetic illusions,” *ACS Photonics* **5**(5), 1718–1725 (2018).

- <sup>41</sup>X.-G. Luo, M.-B. Pu, X. Li, and X.-L. Ma, "Broadband spin Hall effect of light in single nanoperturbations," *Light: Sci. Appl.* **6**(6), e16276 (2017).
- <sup>42</sup>Y. Wang *et al.*, "Staked graphene for tunable terahertz absorber with customized bandwidth," *Plasmonics* **11**(5), 1201–1206 (2016).
- <sup>43</sup>M. Song, H. Yu, J. Luo, and Z. Zhang, "Tailoring infrared refractory plasmonic material to broadband circularly polarized thermal emitter," *Plasmonics* **12**(3), 649–654 (2017).
- <sup>44</sup>M. Pu, Y. Guo, X. Li, X. Ma, and X. Luo, "Revisitation of extraordinary Young's interference: From catenary optical fields to spin-orbit interaction in metasurfaces," *ACS Photonics* **5**(8), 3198–3204 (2018).
- <sup>45</sup>M. Pu *et al.*, "Catenary optics for achromatic generation of perfect optical angular momentum," *Sci. Adv.* **1**(9), e1500396 (2015).
- <sup>46</sup>W. T. Chen *et al.*, "High-efficiency broadband meta-hologram with polarization-controlled dual images," *Nano Lett.* **14**(1), 225–230 (2014).
- <sup>47</sup>F. Ding, Z. Wang, S. He, V. M. Shalaev, and A. V. Kildishev, "Broadband high-efficiency half-wave plate: A supercell-based plasmonic metasurface approach," *ACS Nano* **9**(4), 4111–4119 (2015).
- <sup>48</sup>J. Zhang, J.-Y. Ou, K. F. MacDonald, and N. I. Zheludev, "Optical response of plasmonic relief meta-surfaces," *J. Opt.* **14**(11), 114002 (2012).
- <sup>49</sup>X. Li *et al.*, "Multicolor 3D meta-holography by broadband plasmonic modulation," *Sci. Adv.* **2**(11), e1601102 (2016).
- <sup>50</sup>N. I. Zheludev, S. L. Prosvirnin, N. Papasimakis, and V. A. Fedotov, "Lasing spaser," *Nat. Photonics* **2**(6), 351–354 (2008).
- <sup>51</sup>B. Luk'yanchuk *et al.*, "The Fano resonance in plasmonic nanostructures and metamaterials," *Nat. Mater.* **9**(9), 707–715 (2010).
- <sup>52</sup>G. Si *et al.*, "Reflective plasmonic color filters based on lithographically patterned silver nanorod arrays," *Nanoscale* **5**(14), 6243 (2013).
- <sup>53</sup>T. Xu, Y.-K. Wu, X. Luo, and L. J. Guo, "Plasmonic nanoresonators for high-resolution colour filtering and spectral imaging," *Nat. Commun* **1**(5), 59 (2010).
- <sup>54</sup>H. Lochbihler, "Colored images generated by metallic sub-wavelength gratings," *Opt. Express* **17**(14), 12189 (2009).
- <sup>55</sup>W. Cai *et al.*, "Metamagnetics with rainbow colors," *Opt. Express* **15**(6), 3333 (2007).
- <sup>56</sup>H.-S. Lee, Y.-T. Yoon, S. Lee, S.-H. Kim, and K.-D. Lee, "Color filter based on a subwavelength patterned metal grating," *Opt. Express* **15**(23), 15457 (2007).
- <sup>57</sup>V. R. Shrestha, C.-S. Park, and S.-S. Lee, "Enhancement of color saturation and color gamut enabled by a dual-band color filter exhibiting an adjustable spectral response," *Opt. Express* **22**(3), 3691 (2014).
- <sup>58</sup>V. A. Fedotov *et al.*, "Spectral collapse in ensembles of metamolecules," *Phys. Rev. Lett.* **1** **4**(22), 223901 (2010).
- <sup>59</sup>S. J. Tan *et al.*, "Plasmonic color palettes for photorealistic printing with aluminum nanostructures," *Nano Lett.* **14**(7), 4023–4029 (2014).
- <sup>60</sup>N. Nguyen-Huu, Y.-L. Lo, and Y.-B. Chen, "Color filters featuring high transmission efficiency and broad bandwidth based on resonant waveguide-metallic grating," *Opt. Commun.* **284**(10–11), 2473–2479 (2011).
- <sup>61</sup>A. M. Shalitout, J. Kim, A. Boltasseva, V. M. Shalaev, and A. V. Kildishev, "Ultrathin and multicolour optical cavities with embedded metasurfaces," *Nat. Commun.* **9**(1), 2673 (2018).
- <sup>62</sup>B. Zeng, Y. Gao, and F. J. Bartoli, "Ultrathin nanostructured metals for highly transmissive plasmonic subtractive color filters," *Sci. Rep.* **3**(1), 2840 (2013).
- <sup>63</sup>L. Duempelmann, D. Casari, A. Luu-Dinh, B. Gallinet, and L. Novotny, "Color rendering plasmonic aluminum substrates with angular symmetry breaking," *ACS Nano* **9**(12), 12383–12391 (2015).
- <sup>64</sup>X. M. Goh, R. J. H. Ng, S. Wang, S. J. Tan, and J. K. W. Yang, "Comparative study of plasmonic colors from all-metal structures of posts and pits," *ACS Photonics* **3**(6), 1000–1009 (2016).
- <sup>65</sup>V. R. Shrestha, S.-S. Lee, E.-S. Kim, and D.-Y. Choi, "Aluminum plasmonics based highly transmissive polarization-independent subtractive color filters exploiting a nanopatch array," *Nano Lett.* **14**(11), 6672–6678 (2014).
- <sup>66</sup>H. Lochbihler, "Reflective colored image based on metal-dielectric-metal-coated gratings," *Opt. Lett.* **38**(9), 1398 (2013).
- <sup>67</sup>A. F. Kaplan, T. Xu, and L. J. Guo, "High efficiency resonance-based spectrum filters with tunable transmission bandwidth fabricated using nanoimprint lithography," *Appl. Phys. Lett.* **99**(14), 143111 (2011).
- <sup>68</sup>Y.-T. Yoon, C.-H. Park, and S.-S. Lee, "Highly efficient color filter incorporating a thin metal-dielectric resonant structure," *Appl. Phys. Express* **5**(2), 022501 (2012).
- <sup>69</sup>M. J. Uddin and R. Magnusson, "Highly efficient color filter array using resonant  $\text{Si}_3\text{N}_4$  gratings," *Opt. Express* **21**(10), 12495 (2013).
- <sup>70</sup>J. Olson *et al.*, "Vivid, full-color aluminum plasmonic pixels," *Proc. Natl. Acad. Sci.* **111**(40), 14348–14353 (2014).
- <sup>71</sup>N. S. King *et al.*, "Fano resonant aluminum nanoclusters for plasmonic colorimetric sensing," *ACS Nano* **9**(11), 10628–10636 (2015).
- <sup>72</sup>F. Ding, Y. Yang, R. A. Deshpande, and S. I. Bozhevolnyi, "A review of gap-surface plasmon metasurfaces: Fundamentals and applications," *Nanophotonics* **7**(6), 1129–1156 (2018).
- <sup>73</sup>J. Xue *et al.*, "Scalable, full-colour and controllable chromotropic plasmonic printing," *Nat. Commun.* **6**(1), 8906 (2015).
- <sup>74</sup>W. Li *et al.*, "Refractory plasmonics with titanium nitride: Broadband metamaterial absorber," *Adv. Mater.* **26**(47), 7959–7965 (2014).
- <sup>75</sup>K. Diest, J. A. Dionne, M. Spain, and H. A. Atwater, "Tunable color filters based on metal-insulator-metal resonators," *Nano Lett.* **9**(7), 2579–2583 (2009).
- <sup>76</sup>M. Song, Z. A. Kudyshev, H. Yu, A. Boltasseva, V. M. Shalaev, and A. V. Kildishev, "Achieving full-color generation with polarization-tunable perfect light absorption," *Opt. Mater. Express* **9**(2), 779 (2019).
- <sup>77</sup>D. Wang *et al.*, "Spatial and temporal nanoscale plasmonic heating quantified by thermoreflectance," *Nano Lett.* **19**(6), 3796–3803 (2019).
- <sup>78</sup>M. Miyata, H. Hatada, and J. Takahara, "Full-color subwavelength printing with gap-plasmonic optical antennas," *Nano Lett.* **16**(5), 3166–3172 (2016).
- <sup>79</sup>A. S. Roberts, A. Pors, O. Albrektsen, and S. I. Bozhevolnyi, "Subwavelength plasmonic color printing protected for ambient use," *Nano Lett.* **14**(2), 783–787 (2014).
- <sup>80</sup>W. Wang *et al.*, "Full color generation using silver tandem nanodisks," *ACS Nano* **11**(5), 4419–4427 (2017).
- <sup>81</sup>T. D. James, P. Mulvaney, and A. Roberts, "The plasmonic pixel: Large area, wide gamut color reproduction using aluminum nanostructures," *Nano Lett.* **16**(6), 3817–3823 (2016).
- <sup>82</sup>J. S. Clausen *et al.*, "Plasmonic metasurfaces for coloration of plastic consumer products," *Nano Lett.* **14**(8), 4499–4504 (2014).
- <sup>83</sup>X. Ni, S. Ishii, A. V. Kildishev, and V. M. Shalaev, "Ultra-thin, planar, Babinet-inverted plasmonic metaleenses," *Light: Sci. Appl.* **2**(4), e72 (2013).
- <sup>84</sup>F. Cheng, J. Gao, T. S. Luk, and X. Yang, "Structural color printing based on plasmonic metasurfaces of perfect light absorption," *Sci. Rep.* **5**(1), 11045 (2015).
- <sup>85</sup>L. B. Sun *et al.*, "Influence of structural parameters to polarization-independent color-filter behavior in ultrathin Ag films," *Opt. Commun.* **333**, 16–21 (2014).
- <sup>86</sup>L. B. Sun *et al.*, "Effect of relative nanohole position on colour purity of ultra-thin plasmonic subtractive colour filters," *Nanotechnology* **26**(30), 305204 (2015).
- <sup>87</sup>S. Yokogawa, S. P. Burgos, and H. A. Atwater, "Plasmonic color filters for CMOS image sensor applications," *Nano Lett.* **12**(8), 4349–4354 (2012).
- <sup>88</sup>S. P. Burgos, S. Yokogawa, and H. A. Atwater, "Color imaging via nearest neighbor hole coupling in plasmonic color filters integrated onto a complementary metal-oxide semiconductor image sensor," *ACS Nano* **7**(11), 10038–10047 (2013).
- <sup>89</sup>W. L. Barnes, A. Dereux, and T. W. Ebbesen, "Surface plasmon subwavelength optics," *Nature* **424**(6950), 824–830 (2003).
- <sup>90</sup>Q. Chen and D. R. S. Cumming, "High transmission and low color cross-talk plasmonic color filters using triangular-lattice hole arrays in aluminum films," *Opt. Express* **18**(13), 14056 (2010).
- <sup>91</sup>J. Prikulis, P. Hanarp, L. Olofsson, D. Sutherland, and M. Käll, "Optical spectroscopy of nanometric holes in thin gold films," *Nano Lett.* **4**(6), 1003–1007 (2004).
- <sup>92</sup>L. Lin and A. Roberts, "Angle-robust resonances in cross-shaped aperture arrays," *Appl. Phys. Lett.* **97**(6), 061109 (2010).
- <sup>93</sup>D. Inoue *et al.*, "Polarization independent visible color filter comprising an aluminum film with surface-plasmon enhanced transmission through a subwavelength array of holes," *Appl. Phys. Lett.* **98**(9), 93113 (2011).
- <sup>94</sup>G. Si *et al.*, "Annular aperture array based color filter," *Appl. Phys. Lett.* **99**(3), 033105 (2011).
- <sup>95</sup>L. Martin-Moreno *et al.*, "Theory of extraordinary optical transmission through subwavelength hole arrays," *Phys. Rev. Lett.* **86**(6), 1114–1117 (2001).

- <sup>96</sup>C. Genet and T. W. Ebbesen, "Light in tiny holes," *Nature* **445**(7123), 39–46 (2007).
- <sup>97</sup>J. Hutchinson, "Culture, communication, and an information age Madonna," *IEEE Prof. Commun. Soc. Newslet.* **45**(3), 5–7 (2001).
- <sup>98</sup>T. Zentgraf *et al.*, "Babinet's principle for optical frequency metamaterials and nanoantennas," *Phys. Rev. B* **76**(3), 033407 (2007).
- <sup>99</sup>W. Yue, S. Gao, S.-S. Lee, E.-S. Kim, and D.-Y. Choi, "Highly reflective subtractive color filters capitalizing on a silicon metasurface integrated with nanostructured aluminum mirrors," *Laser Photonics Rev.* **11**(3), 1600285 (2017).
- <sup>100</sup>E. Højlund-Nielsen *et al.*, "Plasmonic colors: Toward mass production of metasurfaces," *Adv. Mater. Technol.* **1**(7), 1600054 (2016).
- <sup>101</sup>T. Ellenbogen, K. Seo, and K. B. Crozier, "Chromatic plasmonic polarizers for active visible color filtering and polarimetry," *Nano Lett.* **12**(2), 1026–1031 (2012).
- <sup>102</sup>Z. Li, A. W. Clark, and J. M. Cooper, "Dual color plasmonic pixels create a polarization controlled nano color palette," *ACS Nano* **1**(1), 492–498 (2016).
- <sup>103</sup>L. Duempelmann, A. Luu-Dinh, B. Gallinet, and L. Novotny, "Four-fold color filter based on plasmonic phase retarder," *ACS Photonics* **3**(2), 190–196 (2016).
- <sup>104</sup>E. Heydari *et al.*, "Plasmonic color filters as dual-state nanopixels for high-density microimage encoding," *Adv. Funct. Mater.* **27**(35), 1701866 (2017).
- <sup>105</sup>X. M. Goh *et al.*, "Three-dimensional plasmonic stereoscopic prints in full colour," *Nat. Commun.* **5**, 5361 (2014).
- <sup>106</sup>M. Song *et al.*, "Wavelength-dependent optical-rotation manipulation for active color display and highly secure encryption," in Conference on Lasers and Electro-Optics (2018), p. FTh4M.2.
- <sup>107</sup>P. Zijlstra, J. W. M. Chon, and M. Gu, "Five-dimensional optical recording mediated by surface plasmons in gold nanorods," *Nature* **459**(7245), 410–413 (2009).
- <sup>108</sup>M. Gu, X. Li, and Y. Cao, "Optical storage arrays: A perspective for future big data storage," *Light: Sci. Appl.* **3**(5), e177 (2014).
- <sup>109</sup>J. Strasswimmer, M. C. Pierce, B. H. Park, V. Neel, and J. F. de Boer, "Polarization-sensitive optical coherence tomography of invasive basal cell carcinoma," *J. Biomed. Opt.* **9**(2), 292 (2004).
- <sup>110</sup>K. Xiong *et al.*, "Plasmonic metasurfaces with conjugated polymers for flexible electronic paper in color," *Adv. Mater.* **28**(45), 9956–9960 (2016).
- <sup>111</sup>D. Franklin, R. Frank, S.-T. Wu, and D. Chanda, "Actively addressed single pixel full-colour plasmonic display," *Nat. Commun.* **8**, 15209 (2017).
- <sup>112</sup>E. Feigenbaum, K. Diest, and H. A. Atwater, "Unity-order index change in transparent conducting oxides at visible frequencies," *Nano Lett.* **1**(6), 2111–2116 (2010).
- <sup>113</sup>Z.-W. Xie, J.-H. Yang, V. Vashistha, W. Lee, and K.-P. Chen, "Liquid-crystal tunable color filters based on aluminum metasurfaces," *Opt. Express* **25**(24), 30764 (2017).
- <sup>114</sup>G. G. Nair *et al.*, "Electrically tunable color by using mixtures of bent-core and rod-shaped molecules," *Adv. Mater.* **2**(16), 3138–3142 (2008).
- <sup>115</sup>S. S. Mirshafieyan and D. A. Gregory, "Electrically tunable perfect light absorbers as color filters and modulators," *Sci. Rep.* **8**(1), 2635 (2018).
- <sup>116</sup>Y. Lee *et al.*, "Electrical broad tuning of plasmonic color filter employing an asymmetric-lattice nanohole array of metasurface controlled by polarization rotator," *ACS Photonics* **4**(8), 1954–1966 (2017).
- <sup>117</sup>J. Xiang *et al.*, "Electrically Tunable Selective Reflection of Light from Ultraviolet to Visible and Infrared by Heliconical Cholesterics," *Adv. Mater.* **27**(19), 3014–3018 (2015).
- <sup>118</sup>C.-H. Park, Y.-T. Yoon, V. R. Shrestha, C.-S. Park, S.-S. Lee, and E.-S. Kim, "Electrically tunable color filter based on a polarization-tailored nano-photonic dichroic resonator featuring an asymmetric subwavelength grating," *Opt. Express* **21**(23), 28783–28793 (2013).
- <sup>119</sup>D. Franklin *et al.*, "Polarization-independent actively tunable colour generation on imprinted plasmonic surfaces," *Nat. Commun.* **6**(1), 7337 (2015).
- <sup>120</sup>N. J. Greybush *et al.*, "Dynamic plasmonic pixels," *ACS Nano* **13**(4), 3875–3883 (2019).
- <sup>121</sup>N. Li *et al.*, "Dynamically switchable multicolor electrochromic films," *Small* **15**(7), 1804974 (2019).
- <sup>122</sup>M. Wang and Y. Yin, "Magnetically responsive nanostructures with tunable optical properties," *J. Am. Chem. Soc.* **138**(20), 6315–6323 (2016).
- <sup>123</sup>X. Wang *et al.*, "Anisotropically shaped magnetic/plasmonic nanocomposites for information encryption and magnetic-field-direction sensing," *Research* **2** **18**, 7527825.
- <sup>124</sup>M. Wang *et al.*, "Magnetic tuning of plasmonic excitation of gold nanorods," *J. Am. Chem. Soc.* **135**(41), 15302–15305 (2013).
- <sup>125</sup>O. L. Muskens *et al.*, "Antenna-assisted picosecond control of nanoscale phase transition in vanadium dioxide," *Light: Sci. Appl.* **5**(10), e16173 (2016).
- <sup>126</sup>M. A. Kats *et al.*, "Vanadium dioxide as a natural disordered metamaterial: Perfect thermal emission and large broadband negative differential thermal emittance," *Phys. Rev. X* **3**(4), 041004 (2013).
- <sup>127</sup>M. A. Kats *et al.*, "Thermal tuning of mid-infrared plasmonic antenna arrays using a phase change material," *Opt. Lett.* **38**(3), 368 (2013).
- <sup>128</sup>F.-Z. Shu *et al.*, "Dynamic plasmonic color generation based on phase transition of vanadium dioxide," *Adv. Opt. Mater.* **6**(7), 1700939 (2018).
- <sup>129</sup>B. Gholipour, A. Karvounis, J. Yin, C. Soci, K. F. MacDonald, and N. I. Zheludev, "Phase-change-driven dielectric-plasmonic transitions in chalcogenide metasurfaces," *NPG Asia Mater.* **1**(6), 533–539 (2018).
- <sup>130</sup>R. Yu *et al.*, "Structural coloring of glass using dewetted nanoparticles and ultrathin films of metals," *ACS Photonics* **3**(7), 1194–1201 (2016).
- <sup>131</sup>X. Chen *et al.*, "Ordered Au nanocrystals on a substrate formed by light-induced rapid annealing," *Nanoscale* **6**(3), 1756–1762 (2014).
- <sup>132</sup>X. Zhu, C. Vannahme, E. Højlund-Nielsen, N. A. Mortensen, and A. Kristensen, "Plasmonic colour laser printing," *Nat. Nanotechnol.* **11**(4), 325–329 (2016).
- <sup>133</sup>M. S. Carstensen, X. Zhu, O. E. Iyore, N. A. Mortensen, U. Levy, and A. Kristensen, "Holographic resonant laser printing of metasurfaces using plasmonic template," *ACS Photonics* **5**(5), 1665–1670 (2018).
- <sup>134</sup>Y. Zhang *et al.*, "Full-visible multifunctional aluminium metasurfaces by in situ anisotropic thermoplasmonic laser printing," *Nanoscale Horiz.* **4**(3), 601–609 (2019).
- <sup>135</sup>S. Raza, C. Lavieja, X. Zhu, and A. Kristensen, "Resonant laser printing of bi-material metasurfaces: From plasmonic to photonic optical response," *Opt. Express* **26**(16), 20203 (2018).
- <sup>136</sup>P. Gadenne, Y. Yagil, and G. Deutscher, "Transmittance and reflectance in situ measurements of semicontinuous gold films during deposition," *J. Appl. Phys.* **66**(7), 3019–3025 (1989).
- <sup>137</sup>P. Nyga, V. P. Drachev, M. D. Thoreson, and V. M. Shalaev, "Mid-IR plasmonics and photomodification with Ag films," *Appl. Phys. B* **93**(1), 59–68 (2008).
- <sup>138</sup>A. S. Roberts *et al.*, "Laser writing of bright colors on near-percolation plasmonic reflector arrays," *ACS Nano* **13**(1), 71–77 (2019).
- <sup>139</sup>P. Nyga *et al.*, "Laser-induced color printing on semicontinuous silver films: Red, green and blue," *Opt. Mater. Express* **9**(3), 1528 (2019).
- <sup>140</sup>M. D. Ooms, Y. Jeyaram, and D. Sinton, "Disposable plasmonics: rapid and inexpensive large area patterning of plasmonic structures with CO<sub>2</sub> laser annealing," *Langmuir* **31**(18), 5252–5258 (2015).
- <sup>141</sup>K. J. Berean *et al.*, "Laser-induced dewetting for precise local generation of au nanostructures for tunable solar absorption," *Adv. Opt. Mater.* **4**(8), 1247–1254 (2016).
- <sup>142</sup>K. Toyoda, K. Miyamoto, N. Aoki, R. Morita, and T. Omatsu, "Using optical vortex to control the chirality of twisted metal nanostructures," *Nano Lett.* **12**(7), 3645–3649 (2012).
- <sup>143</sup>A. Y. Vorobyev and C. Guo, "Enhanced absorptance of gold following multi-pulse femtosecond laser ablation," *Phys. Rev. B* **72**(19), 195422 (2005).
- <sup>144</sup>A. Y. Vorobyev and C. Guo, "Colorizing metals with femtosecond laser pulses," *Appl. Phys. Lett.* **92**(4), 041914 (2008).
- <sup>145</sup>J.-M. Guay *et al.*, "Laser-induced plasmonic colours on metals," *Nat. Commun.* **8**, 16095 (2017).
- <sup>146</sup>G. V. Odintsova, E. A. Vlasova, Y. M. Andreeva, M. K. Moskvin, A. S. Krivonosov, E. V. Gorbunova, D. V. Pankin, O. S. Medvedev, M. M. Sergeev, N. N. Shchedrina, D. S. Lutoshina, and V. P. Veiko, "High-resolution large-scale plasmonic laser color printing for jewelry applications," *Opt. Express* **27**(3), 3672 (2019).
- <sup>147</sup>X. Duan, S. Kamin, and N. Liu, "Dynamic plasmonic colour display," *Nat. Commun.* **8**, 14606 (2017).
- <sup>148</sup>J. Li, S. Kamin, G. Zheng, F. Neubrech, S. Zhang, and N. Liu, "Addressable metasurfaces for dynamic holography and optical information encryption," *Sci. Adv.* **4**(6), eaar6768 (2018).
- <sup>149</sup>Y. Chen *et al.*, "Dynamic color displays using stepwise cavity resonators," *Nano Lett.* **17**(9), 5555–5560 (2017).

- <sup>150</sup>Y. Gao *et al.*, "Lead halide perovskite nanostructures for dynamic color display," *ACS Nano* **12**(9), 8847–8854 (2018).
- <sup>151</sup>S. Malynych and G. Chumanov, "Light-induced coherent interactions between silver nanoparticles in two-dimensional arrays," *J. Am. Chem. Soc.* **125**(10), 2896–2898 (2003).
- <sup>152</sup>Y.-L. Chiang *et al.*, "Mechanically tunable surface plasmon resonance based on gold nanoparticles and elastic membrane polydimethylsiloxane composite," *Appl. Phys. Lett.* **96**(4), 041904 (2010).
- <sup>153</sup>M. G. Millyard, F. M. Huang, R. White, E. Spigone, J. Kivioja, and J. J. Baumberg, "Stretch-induced plasmonic anisotropy of self-assembled gold nanoparticle mats," *Appl. Phys. Lett.* **100**(7), 073101 (2012).
- <sup>154</sup>R. Caputo, U. Cataldi, T. Bürgi, and C. Umeton, "Plasmomechanics: A colour-changing device based on the plasmonic coupling of gold nanoparticles," *Mol. Cryst. Liq. Cryst.* **614**(1), 20–29 (2015).
- <sup>155</sup>S. Rehwald *et al.*, "Tunable nanowires: An additional degree of freedom in plasmonics," *Phys. Rev. B* **76**(8), 085420 (2007).
- <sup>156</sup>F. Lütföld, D. Casari, and B. Gallinet, "Low-cost and large-area strain sensors based on plasmonic Fano resonances," *Adv. Opt. Mater.* **4**(5), 715–721 (2016).
- <sup>157</sup>S. Olcum, A. Kocabas, G. Ertas, A. Atalar, and A. Aydinli, "Tunable surface plasmon resonance on an elastomeric substrate," *Opt. Express* **17**(10), 8542 (2009).
- <sup>158</sup>M. L. Tseng, J. Yang, M. Semmlinger, C. Zhang, P. Nordlander, and N. J. Halas, "Two-dimensional active tuning of an aluminum plasmonic array for full-spectrum response," *Nano Lett.* **17**(10), 6034–6039 (2017).
- <sup>159</sup>S. Song *et al.*, "Actively tunable structural color rendering with tensile substrate," *Adv. Opt. Mater.* **5**(9), 1600829 (2017).
- <sup>160</sup>S. Aksu *et al.*, "Flexible plasmonics on unconventional and nonplanar substrates," *Adv. Mater.* **23**(38), 4422–4430 (2011).
- <sup>161</sup>A. Yang *et al.*, "Programmable and reversible plasmon mode engineering," *Proc. Natl. Acad. Sci.* **113**(50), 14201–14206 (2016).
- <sup>162</sup>R. M. Cole, S. Mahajan, and J. J. Baumberg, "Stretchable metal-elastomer nanovoids for tunable plasmons," *Appl. Phys. Lett.* **95**(15), 154103 (2009).
- <sup>163</sup>X. Zhu, L. Shi, X. Liu, J. Zi, and Z. Wang, "A mechanically tunable plasmonic structure composed of a monolayer array of metal-capped colloidal spheres on an elastomeric substrate," *Nano Res.* **3**(11), 807–812 (2010).
- <sup>164</sup>L. Gao *et al.*, "Optics and nonlinear buckling mechanics in large-area, highly stretchable arrays of plasmonic nanostructures," *ACS Nano* **9**(6), 5968–5975 (2015).
- <sup>165</sup>D. Yoo, T. W. Johnson, S. Cherukulappurath, D. J. Norris, and S.-H. Oh, "Template-stripped tunable plasmonic devices on stretchable and rollable substrates," *ACS Nano* **9**(11), 10647–10654 (2015).
- <sup>166</sup>D. Feng, H. Zhang, S. Xu, L. Tian, and N. Song, "Fabrication of plasmonic nanoparticles on a wave shape PDMS substrate," *Plasmonics* **12**(5), 1627–1631 (2017).
- <sup>167</sup>D. Feng, H. Zhang, S. Xu, L. Tian, and N. Song, "Stretchable array of metal nanodisks on a 3D sinusoidal wavy elastomeric substrate for frequency tunable plasmonics," *Nanotechnology* **28**(11), 115703 (2017).
- <sup>168</sup>U. Cataldi *et al.*, "Growing gold nanoparticles on a flexible substrate to enable simple mechanical control of their plasmonic coupling," *J. Mater. Chem. C* **2**(37), 7927–7933 (2014).
- <sup>169</sup>H. Honma, K. Takahashi, M. Ishida, and K. Sawada, "Continuous control of surface-plasmon excitation wavelengths using nanomechanically stretched subwavelength grating," *Appl. Phys. Express* **9**(2), 027201 (2016).
- <sup>170</sup>K. Yamaguchi, M. Fujii, T. Okamoto, and M. Haraguchi, "Electrically driven plasmon chip: Active plasmon filter," *Appl. Phys. Express* **7**(1), 012201 (2014).
- <sup>171</sup>N. I. Zheludev and E. Plum, "Reconfigurable nanomechanical photonic metamaterials," *Nat. Nanotechnol.* **11**(1), 16–22 (2016).
- <sup>172</sup>H. Honma, K. Takahashi, M. Ishida, and K. Sawada, "Fabrication of tunable plasmonic color filter using al subwavelength grating integrated with electrostatic comb-drive actuator," in 2015 Transducers—2015 18th International Conference on Solid-State Sensors, Actuators and Microsystems (TRANSDUCERS) (2015), pp. 2053–2056.
- <sup>173</sup>H. Honma, M. Mitsudome, M. Ishida, K. Sawada, and K. Takahashi, "Nanooptomechanical characterization of surface-plasmon-based tunable filter integrated with comb-drive actuator," *J. Micromech. Microeng.* **27**(3), 034001 (2017).
- <sup>174</sup>M. Swillam, Y. Ismail, and R. Kotb, "Tunable nanoplasmonics," *Adv. Electromagn.* **2**(2), 1 (2013).
- <sup>175</sup>T. Lee, A. Higo, H. Fujita, Y. Nakano, and H. Toshiyoshi, "A study on color-tunable MEMS device based on plasmon photonics," in 2010 International Conference on Optical MEMS and Nanophotonics (2010), pp. 107–108.
- <sup>176</sup>T. Lee, A. Higo, H. Fujita, Y. Nakano, and H. Toshiyoshi, "Transmissive color shift through layered sub-wavelength gratings based on plasmon enhanced coupling," in 2011 16th International Solid-State Sensors, Actuators and Microsystems Conference (2011), pp. 1542–1545.
- <sup>177</sup>Y. Nagasaki *et al.*, "Optical bistability in shape-memory nanowire metamaterial array," *Appl. Phys. Lett.* **113**(2), 021105 (2018).
- <sup>178</sup>M. Miyata, A. Kajima, Y. Nagasaki, and J. Takahara, "Electromechanically tunable plasmonic nanowires operating in visible wavelengths," *ACS Photonics* **3**(12), 2268–2274 (2016).
- <sup>179</sup>A. Q. Liu, W. M. Zhu, D. P. Tsai, and N. I. Zheludev, "Micromachined tunable metamaterials: A review," *J. Opt.* **14**(11), 114009 (2012).
- <sup>180</sup>Q. Chen *et al.*, "A CMOS image sensor integrated with plasmonic colour filters," *Plasmonics* **7**(4), 695–699 (2012).
- <sup>181</sup>B. Y. Zheng, Y. Wang, P. Nordlander, and N. J. Halas, "Color-selective and CMOS-compatible photodetection based on aluminum plasmonics," *Adv. Mater.* **26**(36), 6318–6323 (2014).
- <sup>182</sup>T. Mauren *et al.*, "The beginnings of plasmomechanics: Towards plasmonic strain sensors," *Front. Mater. Sci.* **9**(2), 170–177 (2015).
- <sup>183</sup>J. Liu and Y. Lu, "Fast colorimetric sensing of adenosine and cocaine based on a general sensor design involving aptamers and nanoparticles," *Angew. Chem. Int. Ed.* **45**(1), 90–94 (2006).
- <sup>184</sup>N. L. Rosi and C. A. Mirkin, "Nanostructures in biodiagnostics," *Chem. Rev.* **105**(4), 1547–1562 (2005).
- <sup>185</sup>L. Guo, L. Chen, S. Hong, and D.-H. Kim, "Single plasmonic nanoparticles for ultrasensitive DNA sensing: From invisible to visible," *Biosens. Bioelectron.* **79**, 266–272 (2016).
- <sup>186</sup>C. M. Niemeyer, "Nanoparticles, proteins, and nucleic acids: Biotechnology meets materials science," *Angew. Chem. Int. Ed.* **40**(22), 4128–4158 (2001).
- <sup>187</sup>A. Tittl, P. Mai, R. Taubert, D. Dregely, N. Liu, and H. Giessen, "Palladium-based plasmonic perfect absorber in the visible wavelength range and its application to hydrogen sensing," *Nano Lett.* **11**(10), 4366–4369 (2011).
- <sup>188</sup>S. Wang *et al.*, "Subcellular resolution mapping of endogenous cytokine secretion by nano-plasmonic-resonator sensor array," *Nano Lett.* **11**(8), 3431–3434 (2011).